New Illumination and Temperature Constraints of Mercury's Volatile Polar Deposits

Colin D. Hamill[1], **Nancy L. Chabot**[1], **Erwan Mazarico**[2], **Matthew A. Siegler**[3], **Michael K. Barker**[2], **Jose M. Martinez Camacho**[4]

[1]Johns Hopkins University Applied Physics Laboratory, Laurel, MD, USA

[2]NASA Goddard Space Flight Center, Greenbelt, MD, USA

[3]Planetary Science Institute, Tucson, AZ, USA

[4]Southern Methodist University, Dallas, TX, USA

Abstract

Images from the Mercury Dual Imaging System (MDIS) aboard the MErcury Surface, Space ENvironment, GEochemistry, and Ranging mission reveal low-reflectance polar deposits that are interpreted to be lag deposits of organic-rich, volatile material. Interpretation of these highest-resolution images of Mercury's polar deposits has been limited by the available topography models, so local high-resolution (125 m pixel^{-1}) digital elevation models (DEMs) were made using a combination of data from the Mercury Laser Altimeter (MLA) and from shape-from-shading techniques using MDIS images. Local DEMs were made for eight of Mercury's north polar craters; these DEMs were then used to create high-resolution simulated image, illumination, and thermal models. The simulated images reveal that the pixel brightness variations imaged within Mercury's low-reflectance deposits are consistent with scattered light reflecting off of topography and do not need to be explained by volatile compositional differences as previously suggested. The illumination and thermal models show that these low-reflectance polar deposits extend beyond the permanently shadowed region, more than 1.0 km in some locations, and correspond to a maximum surface temperature of greater than 250 K but less than 350 K. The low-reflectance boundaries of all eight polar deposits studied here show a close correspondence with the surface stability boundary of coronene ($C_{24}H_{12}$). While coronene should only be viewed as a proxy for the myriad volatile compounds that may exist in Mercury's polar deposits, coronene's surface stability boundary supports the idea that Mercury's low-reflectance polar deposits are composed of macromolecular organic compounds, consistent with the hypotheses of exogenous transport and in situ production.

1. Introduction

Almost three decades ago, Earth-based radar observations by Goldstone and the Very Large Array revealed areas with unusually high radar backscatter within Mercury's north polar region (Slade et al. 1992; Butler et al. 1993). The existence of these radar-bright materials was subsequently identified at Mercury's south pole by observations from the Arecibo Observatory (Harmon & Slade 1992). These radar-bright materials have been interpreted as water ice within the permanently shadowed regions (PSRs) of polar craters because the radar

characteristics closely resemble those observed for the icy Galilean satellites and the Martian polar ice caps. Additionally, some of the locations of these deposits coincide with craters seen from Mariner 10 images of Mercury's polar regions (Harmon et al. 1994, 2001, 2011; Harmon 2007). Early thermal models constructed by Paige et al. (1992) also indicated that Mercury's polar environments are capable of hosting stable water-ice deposits over geologic timescales.

Multiple data sets from the MErcury Surface, Space ENvironment, GEochemistry, and Ranging (MESSENGER) mission have confirmed that these radar-bright materials are predominantly composed of water ice (Chabot et al. 2018a). The spacecraft's neutron spectrometer (NS) found concentrations of hydrogen in Mercury's north polar region that are consistent with models in which Mercury's polar deposits consist primarily of water ice (Lawrence et al. 2013). Maps of shadowed regions derived from Mercury Dual Imaging System (MDIS; Hawkins et al. 2007) and Mercury Laser Altimeter (MLA) data (Cavanaugh et al. 2007) indicated that all major radar-bright deposits are found within regions of permanent shadow in the north (Deutsch et al. 2016) and south (Chabot et al. 2012, 2018b). Reflectance measurements from the MLA data at 1064 nm wavelength (Neumann et al. 2013; Deutsch et al. 2017) and MDIS imaging (Chabot et al. 2014) revealed unusually bright areas in PSRs within about 5° of Mercury's north pole, interpreted to be ice exposed directly at Mercury's surface.

MLA (Neumann et al. 2013) and MDIS (Chabot et al. 2014, 2016) data also revealed some north polar deposits that were much darker than the surrounding regions, and these low-reflectance deposits were much more prevalent than the high-reflectance deposits beyond about 5° from the north pole. Since they coincided in many cases with radar-bright regions, these low-reflectance deposits were interpreted to be thin, tens of centimeters thick, lag deposits of organic-rich, volatile materials that insulate a water-ice layer beneath them (Neumann et al. 2013; Paige et al. 2013). The highest-resolution (<100 m pixel^{-1}) MDIS images of these polar deposits (Chabot et al. 2016) revealed low-reflectance surfaces with sharp boundaries and intriguing brightness variations. Understanding these features can provide key insight into the nature and composition of Mercury's volatile polar deposits, with implications for their age and origin. However, interpretation of the highest-resolution images of Mercury's volatile polar deposits has been limited by the availability of high-resolution topography, illumination, and temperature models. Existing models were primarily concerned about Mercury's north polar region as a whole. At resolutions of 500 m pixel^{-1} and 1 km pixel^{-1} for the topographic (Deutsch et al. 2016) and thermal models (Paige et al. 2013), respectively, the north polar models did not have the resolution necessary for detailed comparison with the high-resolution images of Mercury's low-reflectance polar deposits.

Fortunately, due to MESSENGER's highly eccentric near-polar orbit, the density of MLA tracks around the north pole enables higher-resolution digital elevation models (DEMs) to be made for certain individual north polar craters. For latitudes near 80°N–85°N, local DEMs can be produced at a resolution that is at least four times that of the full polar region models, enabling higher-resolution illumination and thermal models. In this work, we produce local DEMs using MLA data, as well as shape-from-shading (SfS) techniques with MDIS images,

in order to produce 125 m pixel^{-1} models that are now sufficiently resolved for detailed comparison with the highest-resolution MDIS images of Mercury's polar deposits. With this study, we compare our new high-resolution models to a catalog of high-resolution MDIS images in order to constrain the characteristics of Mercury's low-reflectance polar deposits with a precision that has not been previously possible.

2. Methods

2.1. Crater Selection

This work focuses on eight polar craters (Table 1) situated at latitudes between 80°N and 84°N. These craters were chosen primarily because they have low-reflectance deposits imaged at high resolution by the MDIS Wide Angle Camera (WAC; Chabot et al. 2016), and second because they are situated in a high-density region of MLA tracks (Chabot et al. 2018a). Four craters (Bechet, Desprez, Ensor, and Fuller) were chosen because Chabot et al. (2016) analyzed the brightness variations seen within the MDIS images for these craters with the north polar illumination and thermal models available at the time. In particular, Chabot et al. (2016) suggested that the brightness variations within Desprez' low-reflectance polar deposit were evidence of multiple volatiles on the surface, though the study was limited to a north polar thermal model with 1 km pixel^{-1} resolution. The other four craters (Angelou, Jimenez, Josetsu, and Laxness) were chosen because their low-reflectance polar deposits were imaged in clear detail and showcased interesting boundaries and/or brightness variations in the MDIS images.

Figure 1 shows that all eight craters in this study have a PSR according to the north polar illumination model (Deutsch et al. 2016), although there is not always an extensive radar-bright region associated with these PSRs (e.g., Jimenez and Josetsu). The lack of extensive radar-bright regions may be due to thick lag deposits or, alternatively, thin or absent water-ice layers, either of which would explain the highly limited radar return signals in these locations (Deutsch et al. 2016). Regardless of the radar reflectance variability, these eight craters are ideal candidates for this study of Mercury's volatile polar deposits because of their clear low-reflectance deposits in areas of permanent shadow in high-resolution MDIS images.

2.2. DEMs

High-resolution DEMs are the base for all of the derived simulated image, illumination, and thermal models. During MESSENGER's ~4 years of operation around Mercury, MLA acquired over 26 million altimetric range measurements, primarily in the northern hemisphere (Phillips et al. 2018). MLA tracks were used to create local DEMs of all eight north polar craters at resolutions of 125 m pixel^{-1}, considerably higher than the 500 m pixel^{-1} version available for the full north polar region (Deutsch et al. 2016). These models mitigate orbital geolocation errors by using track bundle-adjustment methods, similar to the methods used by Zuber et al. (2012) to correct for spacecraft position knowledge.

After adjusting the MLA tracks and creating high-resolution DEMs using the MLA data alone, we applied photoclinometry techniques to MDIS images to further refine the craters'

terrains. For each crater, we used ~5–10 WAC 750 nm images with resolutions of ~70–150 m pixel^{-1} sampling a range of solar longitudes. We then applied the Ames Stereo Pipeline's SfS tool, which iteratively adjusted the crater topography to match the shading in the images using the MLA-only DEM as an initial guess (Alexandrov & Beyer 2018; Beyer et al. 2018). The resulting hybrid DEMs provide a more complete view that fills in areas not adequately covered by MLA. Maps of slope and slope azimuth (direction of slope relative to north) were also derived for each crater.

The local DEMs for the eight craters in our study provide unprecedented resolution, as seen in the example of Ensor in Figure 2. The north polar DEM (Figure 2(a)) of 500 m pixel^{-1} is highly pixelated, limiting the ability to resolve the brightness variations of a few hundred meters in size seen in the WAC images (Chabot et al. 2016). As expected, the local MLA-only DEM of Figure 2(c) shows additional detail of the topography of the crater at a resolution of 125 m pixel^{-1}. The hybrid MLA+SfS DEM (Figure 2(c)) provides a superior view of the crater by reducing the residual streakiness resulting from gaps between individual MLA tracks. While these hybrid DEMs refine small-scale topographic errors, the differences in the illumination and thermal models are negligible, with both the MLA-only and MLA+SfS DEMs producing consistent model results that are discussed in the next sections.

2.3. Solar Illumination Models

After the high-resolution DEMs were produced for all eight craters, solar illumination models (e.g., Figure 3(b)) were made at 125 m pixel^{-1} following the methodology of Mazarico et al. (2011, 2018) for lunar craters. These solar illumination models employed a double-precision ray-tracing method to determine the fraction of a Mercury solar day (176 Earth days) in which Mercury's polar surface is directly illuminated by any portion of the Sun (Mazarico et al. 2011, 2018). These illumination models treated the Sun as a disk, not a point source, due to the large areal coverage of the Sun in Mercury's sky (Mazarico et al. 2018). We found that ~100 elements are sufficient, after evaluating several simulations with up to several thousand elements to discretize the solar disk. The crater terrain was input from the local DEMs as an unstructured set of triangular elements at 125 m pixel^{-1}, and then solar rays could be traced to each point on the model to determine direct illumination throughout a Mercury solar day (Mazarico et al. 2018). Lower-resolution DEMs covering the whole polar region were used to capture occlusion from far-field obstacles up to 350 km away. For every crater, we also produced a model of the maximum incident solar flux using the same approach as the illumination model.

2.4. Thermal Models

Thermal models were produced following the methodology of Paige et al. (2013), which created a thermal model for Mercury's north polar region at a resolution of 1 km pixel^{-1}. These thermal models used a ray-tracing method that divided Mercury's biannual insolation cycle into 480 equal time intervals (Paige et al. 2013), and treated the Sun as a disk of 128 triangular elements for which the radiance falls off from the center according to the Sun's limb-darkening curve (Negi et al. 1985; Paige et al. 2013). For Mercury's shadowed regions, which are of primary interest in this study, the thermal conditions were calculated using

reradiated infrared radiation from areas that receive direct illumination (Paige et al. 2013). An average surface albedo of 0.04 and emissivity of 0.90 at infrared wavelengths were used to model each crater. These values are consistent with the parameters of Paige et al. (2013), who used an albedo and emissivity of 0.08 and 0.95, respectively, to model Mercury's north polar region. In our study, an average surface albedo of 0.08 was also explored for modeling the crater's sunlit regions, and it was found that surface albedo differences did not meaningfully change the output of the thermal models. This result is consistent with the previous studies of Mitchell & Pater (1994) and Vasavada et al. (1999) that explained the precise values of albedo and emissivity are not critically important for modeling Mercury's thermal environment.

Three of the outputs from the thermal model are the maximum, minimum, and average temperatures for each crater surface element throughout a full Mercury solar day (176 Earth days). Since volatile sublimation is exponentially dependent on temperature (e.g., Schorgofer & Taylor 2007), maximum temperatures experienced by a surface are the most important factor for determining the long-term stability of volatiles on Mercury's surface. Maximum temperature models, such as in Figure 3(c), are used in this study for investigating the thermal boundaries of the low-reflectance polar deposits.

Stability depth models were also produced for water ice, sulfur, anthracene ($C_{14}H_{10}$), and coronene ($C_{24}H_{12}$; e.g., Figure 3(d)), which model the surface depth at which these volatiles would be lost at a sublimation rate less than 1 mm per billion years. Water-ice stability was modeled so that it could be compared with the Arecibo radar reflectance (Harmon et al. 2011). Sulfur stability was modeled because it was suggested prior to MESSENGER results that sulfur may be the primary constituent of Mercury's polar deposits (Sprague et al. 1995), though MESSENGER observations have shown that sulfur is not consistent with the measurements of the polar deposits (Chabot et al. 2018a). Anthracene and coronene were chosen as simple representatives of a family of complex organic materials suggested by Zhang & Paige (2009) to be present in Mercury's cold traps. The constants needed to model these compounds' sublimation rates were readily available due to their relatively simple aromatic ring structure. While there are many organic compounds that could potentially compose Mercury's polar deposits, no other inorganic compounds that are of similar volatility and prevalence have been proposed to exist on Mercury's surface (Zhang & Paige 2009; Neumann et al. 2013; Paige et al. 2013).

In order to model the stability of each volatile, the compound's molecular weight, triple point temperature and pressure, and sublimation enthalpy were required (Siegler et al. 2014). These stability depth models assumed that the surface and near-surface material in these polar craters had the same thermophysical properties as Mercury's average surface material, as characterized by Mitchell & Pater (1994). The models calculated stability depth up to 2.5 m below the surface (Vasavada et al. 1999; Paige et al. 2013), though this study was primarily focused on the stability of volatiles at the surface in order to compare with the low-reflectance surfaces seen in the high-resolution MDIS images. In Figure 3(d), values >2.5 m are plotted as 2.5 m.

2.5.   MDIS Images

MDIS images were able to reveal the PSR surfaces within Mercury's polar craters by saturating the sunlit surfaces (Chabot et al. 2014, 2016). Images of the permanently shadowed surfaces were taken with the WAC broadband filter (WAC-B; 700 nm central wavelength, 600 nm bandpass). The WAC broadband filter was commonly used during MESSENGER's mission to image faint stars, but the broadband filter also provided high sensitivity to the very low levels of light scattered into the PSRs. Surfaces that were directly illuminated by sunlight quickly saturated in the WAC broadband images but the features of the shadowed surfaces were successfully revealed, illuminated by light scattered off nearby topographic features, such as sunlit crater walls. However, these WAC broadband images also required very specific illumination and imaging geometry so that the sunlit surfaces saturated in the image did not compromise the details of the shadowed surfaces (Chabot et al. 2014, 2018a). Consequently, images acquired in support of MESSENGER's campaign to image Mercury's permanently shadowed polar deposits resulted in a mix of images, a fraction of which successfully revealed details of Mercury's permanently shadowed surfaces and many others that did not.

All MDIS images used for this study were accessed via NASA's Planetary Data System. Between 40 and 140 WAC broadband images were taken for each of the eight craters in this study with resolutions better than 125 m pixel^{-1}. Manual inspection of all of these high-resolution WAC broadband images for each crater was conducted in order to identify the images that successfully revealed the low-reflectance surfaces of the polar deposits. In some images, a portion of a crater's polar deposit was saturated from a nearby sunlit region. When MDIS' charge-coupled device (CCD) elements became saturated with electrons, the electrons spilled over into adjacent areas of the image as saturated streaks due to the readout of the CCD. Thus, in order to best reveal surface details in shadowed regions, the shadowed surfaces were targeted to be situated on the edge of the WAC CCD that was read out first, so that the saturated areas did not streak and compromise the rest of the image rows. Figure 4(c) provides an example WAC broadband image that labels the CCD readout edge, the sunlit saturated region, the sunlit central peak, and the resulting streaks that partially compromise the details of the polar deposit's low-reflectance surface.

Overall, 716 WAC broadband images were inspected for this study, and ultimately only 58 of these images were deemed as successful images that revealed unique, high-resolution details of the polar deposits' low-reflectance surfaces. These successful images are listed in Table A1 and represent the catalog of WAC broadband images used in this study. The final catalog includes 5–10 WAC broadband images for each crater that cover the largest range of viewing angles that are available in the full MESSENGER data set. The emission angle, the angle between the spacecraft and a vector drawn perpendicular to the planet's surface (surface normal), ranges from 0.1° to above 30° for some craters. The incidence angle, the angle between the Sun and the surface normal, ranges narrowly from 80° to 87° since this value is heavily dependent on each crater's latitudinal value. The phase angle, the angle between the Sun and the spacecraft at a point on Mercury's surface, ranges from 45° to 123°. A range of viewing angles is important because it can help to discern the origin of certain brightness variations within the images of each polar deposit.

After gathering the broadband images, the next step was to register the images to their respective high-resolution DEM and local models. To do this, every image and model for an individual crater were mapped to the same projection at the same resolution. Using United States Geological Survey's Integrated Software for Imagers and Spectrometers (USGS ISIS; Gaddis et al. 1997), all images and models were mapped to a polar stereographic projection. The resolution of each image and model was then interpolated to match the highest-resolution WAC broadband image for each crater in order to preserve the highest-resolution images of each crater. The images and models were interpolated to higher resolutions using cubic convolution interpolation methods (Keys 1981) within USGS ISIS; bilinear interpolation methods were analyzed as a potential option and produced essentially the same results. After interpolation, all images and models for a given crater were trimmed to the same spatial extent in order to unify the spatial boundaries of each image and model. If a WAC broadband image did not cover the entire region specified by these spatial parameters, the image was artificially expanded with null values on each side of the image so that the pixel count matched that of the models.

In this study, the high-resolution DEMs were used to indicate the latitudinal and longitudinal positions of each crater. Due to slight errors in spacecraft position knowledge and pointing parameters, the MDIS images had to be manually shifted in order to best align with the local DEMs. To best align the WAC broadband images to the DEMs, an additional WAC narrowband image (WAC-G; 748.7 nm central wavelength, 5.1 nm bandpass) was gathered for each crater (Table A1). The WAC narrowband images that were chosen imaged the entire crater during times of maximum sunlight. These images worked as an intermediary step to best align the broadband images with the models. The WAC narrowband image was registered to the DEM, and then the WAC broadband images were registered to the narrowband image. Since the WAC narrowband images provided a view of each crater at a similar resolution to the broadband images, the narrowband images provided an opportunity to register the broadband images using the smallest features available within the images. Manual registration of the WAC broadband images focused on using physical features, such as small craters and ridges, rather than pixel brightness variations. Since the brightness variations were not known at the time to be caused by topography or physical brightness differences on the surface, small physical features within the crater provided the best way to register the images to the DEM in an unbiased manner.

Because the WAC broadband filter aboard MESSENGER was primarily used to obtain calibration images of stars, this broadband filter was not calibrated for quantitatively determining the reflectance of Mercury's surface (Denevi et al. 2018). For the WAC broadband images used in this study, the raw digital number (DN) values were corrected for dark current, smear, and nonlinearity but no further corrections were applied. The WAC narrowband filters, however, were calibrated for imaging Mercury's surface, and the narrowband images were fully corrected for dark current, smear, nonlinearity, and uniformity (flat field), and then converted to radiance factor (I/F) using USGS ISIS' "mdiscal" function (Denevi et al. 2018).

2.6.   Simulated Images

The high-resolution DEMs were also used to simulate the MDIS WAC broadband images used in this study. These simulated images used the same approach as the solar illumination models by modeling scattered sunlight into the craters' shadowed regions by assuming a surface of uniform albedo (Mazarico et al. 2018); but unlike the solar illumination model that was run for a full Mercury solar day, the time and conditions of each simulated image were chosen to match each specific WAC broadband image. We assumed a Lambertian surface and phase function (Lambert 1760). Photometric models by Domingue et al. (2019) were also investigated for the simulated images and produced qualitatively similar results. The simulations predict the radiance (W m^{-2} sr^{-1} μm^{-1}) observed by MDIS at the time and position that the images were taken during its orbit around Mercury (Mazarico et al. 2018). The radiance calculation depends on the input solar flux, the Mercury–Sun geometry, and the average reflectivity properties of the planet's surface (Mazarico et al. 2018).

Simulated images are key to understanding the small-scale brightness variations seen within the images of each crater's permanently shadowed surface, especially given the complicated illumination conditions with grazing illumination scattered into the scene from many different directions. If a simulated image, which assumes uniform surface albedo, reproduces a WAC broadband image well, then this is an indication that pixel brightness variations in the images are consistent with those expected due to topography and viewing geometry effects. Conversely, if a simulated image does not reproduce the pixel brightness variations in the WAC broadband image, then this is evidence that reflectance variations on the crater's surface are potentially causing the observed pixel brightness variations. Due to computational reasons, only pixels within a region of interest chosen to encompass the PSR were evaluated for scattered light in most simulated images. However, the simulations allow for scattered light from all pixels of the high-resolution DEMs, even those outside of this region of interest. Simulated images were produced that correspond to all 58 WAC broadband images used in this study.

2.7.   Full Data Set for Each Crater

The final data set for each crater is arranged into a three-dimensional array in USGS ISIS, better known as an image cube. Each layer within a cube is registered to one another; the local models provide the reference for co-registration with the MDIS images. Each of the eight cubes contains the following data for each crater: high-resolution MLA+SfS DEMs, average solar illumination, maximum incident solar flux, slope, slope azimuth, surface temperature (maximum, average, and minimum), volatile stability depth (water ice, anthracene, coronene, and sulfur), simulated images, one WAC narrowband image, and WAC broadband images. MLA-only DEMs are also provided for every crater except for Fuller and Laxness since the MLA+SfS DEMs were marginally preferred by the time models were made for these two craters. These fully processed cubes, as well as the raw tagged image file format (TIFF), generic mapping tools grid (GRD), and disk image (IMG) files that were used to produce the cubes, are available for download at the link found in the Acknowledgments.

3. Results

3.1. Brightness Variations in Polar Deposit Images

One of our motivations for creating these high-resolution models is to investigate the origin and nature of the stark brightness variations and boundaries seen in the MDIS images of the low-reflectance polar deposits. Simulated images allow us to do this through comparison with the WAC broadband images.

Figure 4(a) shows the simulated image for EW1067123925B of Fuller, a 27 km diameter crater located at a latitude of 82.6°N. Figure 4(b) outlines the dark regions that have a radiance value less than 0.015 W m^{-2} sr^{-1} μm^{-1}. This value was chosen because it displays a clear boundary between many of the bright and dark regions seen in the simulated image. Similar thresholds were used for the other craters, although variations of about ±0.01 W m^{-2} sr^{-1} μm^{-1} were used to account for the unique illumination conditions of each crater.

Figure 4(c) is image EW1067123925B and Figure 4(d) is the same image of Fuller with the dark outlines from the simulation overlaid on top of the WAC image. Figure 4(d) qualitatively shows how the simulated image predicts the relative pixel brightness variations within the WAC image of Fuller. The similarity between the simulated image and the WAC image is evidence that the vast majority of the pixel brightness variations within the PSR are consistent with those expected due to scattered light reflected off of topography.

The low-reflectance boundary, indicated by the purple arrows in Figure 4(c), has long been interpreted to be the boundary at which low-reflectance volatile compounds cease to exist within Fuller due to the thermal environment within this crater (Chabot et al. 2014, 2016). The fact that this boundary is not visible near the same purple arrows shown within the simulated image in Figure 4(b) is strong evidence that this low-reflectance boundary is indeed the result of physical albedo differences on the surface of Fuller.

Ratios between WAC images (e.g., Figure 4(c)) and their respective simulated images (e.g., Figure 4(a)) were also calculated to conduct a more quantitative comparison. However, such comparisons were not straightforward due to the lack of absolute reflectance calibration of the WAC broadband images. The WAC broadband image has minimally processed DN values, as discussed in Section 2.5, and the simulated image was produced in units of radiance observed by MDIS. Thus, a simple ratio of the WAC and simulated images did not result in a useful quantitative comparison without applying additional factors to account for the uncalibrated pixel values of the WAC image. Instead of synthetically stretching the simulated image values to better match the DN values of the images, or vice-versa, it seemed favorable to just use the qualitative comparisons between the simulated and WAC images, as shown in Figure 4, as that was adequate to address our science question. Figure 4 convincingly shows that the low-reflectance boundary of the polar deposit that is visible in the WAC image is not due to the viewing geometry or surface topography but rather represents a true surface albedo feature. However, many of the other pixel brightness variations within the WAC image of Fuller in Figure 4 are consistent with the brightness variations in the simulated image, providing strong evidence that these pixel brightness

variations do not need to be explained by surface albedo variations within Fuller's low-reflectance polar deposit.

As another example, Figure 5(a) is the simulated image EW1068375172B of Desprez, a 47 km diameter crater located at a latitude of 81.1°N. Figure 5(b) outlines the bright regions of the simulated image that have a radiance greater than 0.015 W m^{-2} sr^{-1} μm^{-1}, a value chosen because it separates the distinct bright and dark regions seen in the simulated image. Figure 5(c) shows WAC image EW1068375172B, and the simulated image outlines are overlaid on top in Figure 5(d). Chabot et al. (2016) analyzed a very similar image of Desprez as shown in Figure 5(c) and showed that the pixel brightness variations in the WAC image are correlated with the maximum surface temperature variability within this crater. They suggested that the brightness variations within the WAC image were evidence of different low-reflectance volatiles on Desprez' surface. However, our new simulated images, as seen in Figure 5, show that sunlight doubly scattered off of Desprez' topography is broadly consistent with the pixel brightness variations seen in this WAC image. Therefore, there is no need to invoke the presence of multiple volatiles to explain the pixel brightness variations seen in the WAC images of Desprez' polar deposit.

In contrast, the purple arrows in Figure 5(c) indicate the low-reflectance boundary of the polar deposit in Desprez. The absence of this low-reflectance polar deposit boundary within the simulated image (Figure 5(b)) strongly supports that this boundary is due to a change in surface albedo within Desprez, as opposed to viewing geometry effects or sunlight reflected off the neighboring topography.

In addition, MLA reflectance data provide direct measurements of the albedo of Mercury's surface and have shown that Mercury's low-reflectance polar deposits are about half as reflective as Mercury's average surface (Neumann et al. 2013; Deutsch et al. 2017). MLA data thus provide an independent method by which to evaluate surface reflectance variations within individual polar deposits. Due to the limited MLA point measurements within the relatively small (<30 km diameter) craters in this study and the inherent MLA absolute reflectance measurement variability (Deutsch et al. 2017), analysis of MLA reflectance within the majority of the craters in our study was limited and inconclusive. Desprez, however, is the largest crater in this study and hosts the largest (>2 km) WAC pixel brightness variations within any one crater's polar deposit. Comparison of the histograms of MLA reflectance values between the bright and dark regions, as defined by the red outlines in Figure 5(b) but confined to the PSR area, showed no reflectance differences between the two regions. Within Desprez' PSR, the bright regions had an average MLA reflectance value of 0.091 ± 0.045 (1σ), while the dark regions had an average value of 0.094 ± 0.044 (1σ). Thus, the MLA reflectance data further support our conclusion that the pixel brightness variations seen in WAC images within Desprez' low-reflectance polar deposit are caused by scattered sunlight variations across the scene and do not represent actual surface reflectance differences.

Simulated images were also used for the analysis of small regions within the PSRs of Bechet, Ensor, and Laxness that had high pixel values, which have been interpreted to be excavated material as a result of ejecta from small craters (<a few kilometers in diameter)

within Mercury's low-reflectance polar deposits (Deutsch et al. 2019). The simulated images suggest that these small-scale bright spots within the images for these three craters are correlated to regions within the image that had the highest scattered light intensity during the times of the WAC images. However, these pixel brightness variations within these craters are on the order of 200–600 m, and the simulated images are at a resolution of 125 m pixel^{-1}, the same resolution as the local DEMs. Thus, our local DEMs and the simulated images produced from them are insufficiently resolved to make conclusive statements about these small-scale brightness variations seen in the WAC images of these three craters in particular. The WAC images and one simulated image for Bechet, Ensor, and Laxness are shown in the Appendix.

Also noteworthy and in contrast to the other seven craters in this study, Josetsu is an old and battered crater, which was chosen for this study because of intriguing brightness variations displayed in WAC broadband images of the crater's permanently shadowed surface. However, our simulated images show that the degraded nature of Josetsu's surface makes it very challenging to discern between brightness variations due to topography and scattered illumination conditions and low-reflectance boundaries due to the presence of low albedo surfaces. Simulated images of Josetsu show that its battered topography has a strong effect on brightness variations within the WAC broadband images. The WAC images and one simulated image for Josetsu are shown in the Appendix.

Overall, the simulated images show that topography plays a large role in producing pixel brightness variations seen in the WAC broadband images. There are many more simulated images for the other WAC images in the final catalog that reach the same conclusion, and these simulated images are provided in the data archive for this study. The high-resolution simulated images, which assume uniform surface albedo, reproduce the large-scale brightness variations of the WAC images well within the low-reflectance polar deposits, suggesting that the pixel brightness variations in these images are consistent with scattered light variations as a result of surface topography. In contrast, the sharp boundaries of the low-reflectance polar deposits are not present in the simulated images, providing strong and compelling evidence that the low-reflectance boundaries of the polar deposits revealed in the MDIS images are due to surface reflectance differences.

3.2. Low-reflectance Polar Deposit Boundaries

Another motivation for creating these high-resolution models is to investigate the locations of the boundaries of the low-reflectance polar deposits seen within these eight craters. Previous models were not resolved enough to investigate the sharp boundaries of Mercury's volatile polar deposits, but the high-resolution models of this study enable such an investigation for the first time. With our new high-resolution models, comparisons can now be made between the WAC broadband images and the high-resolution models in order to find similarities between illumination and thermal boundaries and the polar deposits' low-reflectance boundaries.

Images EW1051458815B (Figure 6(a)) and EW1046946306B (Figure 6(d)) show Ensor's low-reflectance polar deposit, covering both the east and west boundaries. Figures 6(b) and (e) overlay the modeled PSR boundary, and these figures show that the low-reflectance

boundary in both WAC images extends beyond the PSR for both the western side (Figure 6(b)) and the eastern side (Figure 6(e)) of the polar deposit. These complementary images of Ensor that depict both edges of the low-reflectance polar deposit show that Ensor hosts a low-reflectance polar deposit that extends farther out than the PSR in both directions. The low-reflectance boundary extends slightly past Ensor's PSR, ~1.0 km for the northern boundary as is seen in Figure 6(b) and around 500 m for the other sides of the low-reflectance region shown in Figures 6(b) and (e). This offset between the low-reflectance deposit boundary and the PSR cannot be resolved by shifting the WAC images since the PSR is smaller than the low-reflectance polar deposit on all sides. There is no further manual registration that could resolve this fundamental size difference.

As seen in Figures 6(c) and (f), the 250 K maximum surface temperature outline (green) aligns slightly inward of the low-reflectance deposit boundary while the 300 K maximum surface temperature outline (blue) aligns well with the polar deposit boundary. The 350 K maximum surface temperature outline begins to curve and deviate from the expected low-reflectance deposit boundary as seen in the southwestern portion of Figure 6(c) and the southeastern portion of Figure 6(f). It is difficult to pinpoint an exact maximum surface temperature because of the lack of a distinct low-reflectance boundary for Ensor's northern region as seen in Figures 6(c) and (f), so a range of maximum surface temperatures greater than 250 K but less than 350 K is concluded for Ensor's low-reflectance polar deposit. There is a steep temperature gradient around Ensor's polar deposit boundary, but a maximum surface temperature between 250 and 350 K is a meaningful thermal constraint that can be placed on Ensor's volatile polar deposit using these high-resolution models.

Comparison between maximum incident flux and maximum surface temperature in Ensor (Figure 7) shows an expected correlation between the two variables. While maximum incident fluxes for the sunlit surface of Ensor can reach as high as 9000 W m^{-2} and correlate to surface temperatures up to 600 K, Figure 7 focuses on the maximum incident fluxes that correspond to 250–350 K. However, there is a notable spread between maximum incident fluxes and surface temperatures. This spread between these variables is due to the fact that the maximum incident flux models do not take reradiated infrared radiation into account, while the thermal models do. While direct solar flux values are one of the main factors for Ensor's thermal environment, reradiated energy off of nearby sunlit surfaces plays a key role in determining Ensor's maximum surface temperatures for areas that receive little to no direct solar flux or areas that only see a portion of the solar disk. The maximum incident solar flux is an important contributor but is only one factor in determining the thermal environment even for the locations of the low-reflectance deposits that extend beyond the PSR.

The thermal models also provide insight into the surface stability of different volatile compounds, as shown in Figure 8. Figure 8(a) illustrates the surface stability boundaries for elemental sulfur (S) and shows how sulfur may be present in the colder regions of Ensor's polar deposits. However, sulfur is too volatile to be composing the entirety of Ensor's low-reflectance polar deposit. Similarly, Figure 8(b) illustrates the surface stability boundary for anthracene ($C_{14}H_{10}$), a polycyclic aromatic hydrocarbon with a molecular mass of 178 g mol^{-1}. Anthracene is a compound that is stable at the surface for the large majority of the

area within Ensor's low-reflectance polar deposit, though its stability does not match the low-reflectance deposit boundaries seen in the WAC broadband image in some locations, in particular along the northern polar deposit boundary in Figure 8(b). As seen in Figure 8(c), Ensor's low-reflectance region aligns well with the surface stability boundary for coronene ($C_{24}H_{12}$), also a polycyclic aromatic hydrocarbon but with a molecular mass of 300 g mol^{-1}. While coronene is a striking match to the low-reflectance polar deposit boundary in Ensor, thermal sublimation varies approximately with molecular mass (Zhang & Paige 2009, 2010), so it should be viewed as representative of complex organic compounds with molecular masses around 300 g mol^{-1} rather than a specific identification of the low-reflectance material in this crater. The strong match of the coronene stability boundary to the sharp low-reflectance boundary seen in the WAC broadband image of Ensor supports the hypothesis that Mercury's volatile polar deposits are filled with heavy hydrocarbons and other organic compounds. Since the surface stability boundary for coronene is slightly smaller than the low-reflectance polar deposit in Ensor, such as seen in the north–northwestern portion of Figure 8(c), the boundary also suggests that organic compounds with slightly less volatility than coronene may exist within Ensor's low-reflectance polar deposit.

As another example, image EW1053866171B of Jimenez' permanently shadowed interior (Figure 9(a)) showcases the crater's large low-reflectance polar deposit. This image alone captures multiple boundaries of Jimenez' low-reflectance polar deposit and therefore provides an ideal image to use to highlight the conclusions regarding the polar deposit's boundary for Jimenez. As seen in Figure 9(b), the PSR falls around 250 m short of the polar deposit's low-reflectance boundary at the southern side of the image and over 1.0 km short of Jimenez' low-reflectance polar deposit boundary on the eastern side of the image. This low-reflectance boundary corresponds nicely with a maximum surface temperature of 300 K (blue), and the 250 K maximum surface temperature outline (green) falls just a couple hundred meters inward of the low-reflectance polar deposit on the northern and western sides (Figure 9(c)). The extended, nonlinear 350 K maximum surface temperature outline (purple) on Jimenez' southern side, however, suggests that 350 K is too high of a temperature for Jimenez' low-reflectance polar deposit. Although this WAC image in particular shows nearly the entire low-reflectance polar deposit of Jimenez in great resolution (75 m pixel^{-1}), the steep gradient of Jimenez' thermal boundary prevents us from making more exact temperature constraints regarding the low-reflectance volatile polar deposit. This low-reflectance volatile boundary also aligns nicely with the surface stability boundary of coronene (Figure 9(d)), though it should be stressed again that coronene is one proxy for the myriad volatile compounds that could exist within Mercury's polar deposits.

Images for the other five craters with similar PSR and thermal boundaries are included in the Appendix, and each of these craters bears the same results as Ensor and Jimenez. Angelou, Bechet, Desprez, Fuller, Josetsu, and Laxness all have low-reflectance volatile polar deposits that extend in some locations at least 250 m beyond the PSR and match well with a maximum surface temperature boundary between 250 and 350 K. As seen in the 250 K maximum surface temperature outline for Ensor (Figure 6(c)) and the imperfect 250 K maximum surface temperature outlines for Angelou and Fuller, 250 K is too low for the possible maximum surface temperature for Mercury's low-reflectance polar deposits. Conversely, the too-large 350 K maximum surface temperature outlines for the eight craters

in this study demonstrate that this temperature is too high for the maximum surface temperature for Mercury's polar deposits. In all WAC broadband images of the eight polar craters in this study, a maximum surface temperature of roughly 300 K provides the best outline match to the low-reflectance polar deposits.

The similarity between the low-reflectance deposits' thermal boundaries implies that all eight craters host similar volatile compositions. However, previous studies that have inferred organic compounds as the identity of Mercury's low-reflectance volatile deposits have also suggested that Mercury's cold traps do not contain a single low-reflectance volatile compound but rather contain a large number of organic volatile compounds intermixed together, delivered by asteroids or comets (Zhang & Paige 2009; Neumann et al. 2013; Paige et al. 2013) or produced in situ by galactic cosmic rays (Crites et al. 2013; Delitsky et al. 2017). Thus, while our study shows a consistent maximum temperature for the low-reflectance volatile deposits across all eight craters, myriad volatile organic compounds with that maximum volatility temperature or lower may compose Mercury's low-reflectance polar deposits. Nevertheless, though multiple volatile compounds may be present, the volatiles within these polar deposits do not show evidence for any brightness variations in the MESSENGER images beyond those that can be explained by topography-induced light scattering, as discussed in Section 3.1.

Quantitative analysis of the illumination and temperature conditions near the polar deposit boundaries of the eight craters in this study was also performed (Figure 10). By using transects (e.g., Figures 6 and 9), small rectangular boxes that run perpendicular to a small region of a polar deposit boundary, we can sample and compare MDIS pixel values from one broadband image with values of the high-resolution models. In Figure 10, eight transects sample a small region within each of the eight polar craters in order to illustrate the maximum surface temperatures and average illumination conditions immediately surrounding the polar deposit boundaries. For simplicity, the boundary of each craters' PSR, taken as the last instance that the average direct illumination models reported a value of zero (red), was set at a distance of zero on the x-axis. As seen by the MDIS pixel values (blue) in Figure 10, the polar deposit boundary cannot be pinpointed to a precise pixel location, due to the inherent scattering of light from adjacent MDIS pixels (Denevi et al. 2018) and the extended region of the polar deposit boundary as noted in previous work (Chabot et al. 2016). For this reason, the polar deposit boundaries in these plots are represented by blue shaded regions of 100–200 m width and are defined as the region where MDIS pixel values (blue) have the highest rate of change. These regions of high slope represent the pixel value transitions from the low-reflectance deposit to the bright sunlit surrounding region.

As expected from Figures 6 and 9, each polar deposit boundary typically falls 200–750 m from the PSR in the plots in Figure 10, though other locations show deposit boundaries that extended beyond 1.0 km from their respective PSR. The maximum surface temperatures (black) within each blue shaded region, which depicts the low-reflectance polar deposit boundary as determined by the WAC pixel values, are approximately 250–350 K, though there are values that slightly extend beyond this range in either direction. The fact that maximum surface temperatures of roughly ~300 K fall within the blue shaded regions of every plot in Figure 10 is strong confirmation that this temperature is consistent with

constraining the low-reflectance polar deposits for all eight craters in this study. The average direct illumination values (red) show that average illumination varies greatly across different polar deposit boundaries, supporting the idea that maximum incident solar flux is just one factor in determining the thermal constraints of Mercury's polar deposits, as illustrated in Figure 7. Nonetheless, these illumination results suggest that Mercury's low-reflectance volatile polar deposits can survive tens of hours of direct grazing sunlight from a fraction of the solar disk in a Mercury solar day. These hours of direct sunlight are from a portion of the solar disk, yet this amount of direct illumination does not heat Mercury's surface to a maximum surface temperature above 350 K.

The low-reflectance polar deposits also align remarkably well with the surface stability boundary of the heavy (300 g mol^{-1}) organic compound coronene ($C_{24}H_{12}$) for all eight craters in this study. Coronene's surface stability boundary supports the hypothesis that Mercury's low-reflectance volatile polar deposits may be composed of heavy organic compounds, and coronene is just one example used for a vast array of hydrocarbons and other organic compounds with similar volatilities. The north–northwestern coronene surface boundary of Ensor's polar deposit (Figure 8(c)), however, shows that the true low-reflectance volatile boundary may host compounds with slightly less volatility than coronene as well. As seen in the Appendix, Fuller also has a mismatch between the coronene boundary and the low-reflectance boundary of the polar deposit, particularly in the northwestern portion of the PSR. This coronene stability boundary in Fuller highlights how coronene is a close but imperfect approximation of the compounds observed in Mercury's volatile polar deposits. Ensor's and Fuller's imperfect coronene boundaries suggest that compounds stable to slightly higher temperatures, such as heavier polycyclic aromatic hydrocarbons, may likely be contributing to Mercury's low-reflectance volatile polar deposits along with many more volatile compounds like anthracene and coronene.

4. Conclusions and Implications

Due to MESSENGER's highly eccentric near-polar orbit, the density of MLA tracks around the north pole enables higher-resolution, local DEMs to be made for individual north polar craters. These high-resolution (125 m pixel^{-1}) DEMs were created for eight north polar craters at latitudes between 80°N and 84°N, and these DEMs were then used to create high-resolution simulated images and illumination and thermal models. These models were compared to the high-resolution WAC broadband images of Mercury's low-reflectance polar deposits in order to interpret the nature of the brightness variations and low-reflectance boundaries seen within the images of these polar craters.

The simulated images, which assume uniform surface albedo, match the brightness variations of the WAC broadband images very well, suggesting that these pixel brightness variations within Mercury's low-reflectance polar deposits are the result of topography-induced light scattering and viewing geometry effects. However, these simulated images do not reproduce the polar deposits' low-reflectance boundaries imaged within these craters, and this provides strong confirmation that these boundaries are the result of surface albedo differences caused by low-reflectance volatile compounds within the craters' cold traps.

The low-reflectance polar deposits within these craters extend beyond the PSRs of each crater by at least 250 m, and for distances beyond 1.0 km. The low-reflectance boundaries of the polar deposits correspond to a maximum surface temperature of greater than 250 K and less than 350 K, with a maximum surface temperature of roughly 300 K providing a good match for all eight craters in this study. The fact that the 250–350 K maximum surface temperatures are the best-fit for all eight polar craters supports that the volatile species are the same, or at least very similar, for all of these craters' polar deposits.

Solar insolation varies with longitude because of Mercury's eccentric orbit and 3:2 spin–orbit resonance (Colombo & Shapiro 1966). Previous studies have shown that surface temperatures are more hospitable for water ice and other volatiles near the cold-pole longitudes at lower latitudes (Harmon et al. 2001, 2011; Harmon 2007; Chabot et al. 2013). In this study, the eight craters span longitudes that cross the cold-pole at 270°E, but all eight craters reveal consistent results to constrain the maximum surface temperature of the polar deposits' thermal boundaries, showing no additional longitudinal effect of the neighboring hot-pole or cold-pole longitudes. This is consistent with the study of Deutsch et al. (2016) that found no meaningful hot-pole or cold-pole patterns within 10° latitude of the north pole, the region where the eight craters of our study are located.

The polar deposits' low-reflectance boundaries align well with the surface stability boundary of coronene ($C_{24}H_{12}$), which is a useful proxy for the multitude of volatile organic compounds that have been suggested to compose each craters' low-reflectance volatile polar deposit. These maximum surface temperature constraints for Mercury's polar deposits, along with the surface stability boundaries for coronene, provide important new evidence supporting that Mercury's low-reflectance polar deposits may be filled with hydrocarbons and other volatile organic compounds. Primitive bodies, such as asteroids, comets, and micrometeoroids, are thought to contain a wide range of volatile compounds such as aromatic hydrocarbons, linear amides, and carboxylic acids (Zhang & Paige 2009). Polycyclic aromatic hydrocarbons (e.g., coronene) and other macromolecular organic compounds are stable to temperatures greater than 250 K and have been observed to be present in comets and meteorites (Kovalenko et al. 1991; Clemett & Zare 1997; Botta & Bada 2002; Clemett et al. 2010). The 250–350 K maximum surface temperature constraints of this study are consistent with the notion that Mercury's low-reflectance polar deposits are composed of organic compounds delivered via volatile-rich comets, asteroids, and/or micrometeoroids (Neumann et al. 2013; Paige et al. 2013). However, energetic particle deposition as a result of galactic cosmic rays, solar energetic particles, and Mercury's magnetosphere may also be inducing chemical reactions within Mercury's polar deposits that yield heavier-weight organic products consistent with the volatility constraints of this study (Crites et al. 2013; Delitsky et al. 2017). It is also possible that both of these processes are occurring, with the delivery of volatile organic compounds to Mercury via small- or large-impact events along with in situ processing once on the surface of Mercury. Our results provide strong evidence that complex organic compounds, such as polycyclic aromatic hydrocarbons, are consistent with the low-reflectance volatiles observed to occupy Mercury's extensive polar cold traps.

In addition to providing constraints on the thermal conditions, and hence identity, of the low-reflectance volatiles in Mercury's polar deposits, the new models of this study can also be used to inform BepiColombo's upcoming investigations. In particular, our results indicate that there are certain times and locations throughout a Mercury solar day where specific portions of specific low-reflectance polar deposits are dimly, but directly, sunlit. Similarly, the illumination models (e.g., Figure 3(b)) illustrate that there are potentially small-scale, dimly lit volatile deposits lying just outside of some crater walls as well. Such times of direct illumination can provide unique opportunities for BepiColombo's imaging instruments to target observations of these locations, potentially enabling spectral and other measurements potentially not feasible without direct illumination, as suggested by Filacchione et al. (2020). Identifying and including these possible imaging opportunities in BepiColombo's operational plans is highly worthwhile to uniquely advance the investigations of the volatiles contained in Mercury's polar cold traps.

Appendix

Table A1 is the catalog of WAC broadband images and WAC narrowband images used for each crater with their pixel resolutions and emission, incidence, and phase angles. Figure A1 showcases all eight high-resolution DEMs produced by this study. Figures A2–A9 show all of the WAC broadband images listed in Table A1 for each crater. Figures A10–A15 depict comparisons between a representative simulated image and its respective WAC broadband image for all craters not showcased in Section 3.

Figure A16 is an example of a ratio taken between a simulated image and its respective WAC broadband image for Desprez. Since a simple division between the simulated image and WAC broadband image was not straightforward due to the lack of absolute reflectance calibration of the WAC broadband image, the ratio image (Figure A16(c)) was made by artificially stretching the WAC broadband DN values to match that of the simulated image. By finding the average value of the brightest region for both the simulated image and WAC broadband image, then finding the average value of the darkest region for both the simulated image and WAC broadband image, a linear equation was found that relates the rate of change of the WAC broadband image with respect to the simulated image. This linear equation was then applied to the WAC broadband image in order to produce a spread of values for the WAC broadband image that is very similar to the spread of values seen in the

simulated image. Then, this stretched WAC broadband image was divided by the simulated image to produce the ratio seen in Figure A16(c).

For Figure A16(a), the value used for the dark region of the WAC image was 351.53 DN, and the value for the brightest region of the WAC image was 435.71 DN. For the respective simulated image in Figure A16(b), a value of 0.000 171 W m^{-2} was used for the darkest regions of the crater, and a value of 0.0216 W m^{-2} was used for the brightest region. These four values were used to find a slope (Δ image values/Δ simulation values) of 3928.3 and y-intercept of 5.1 that was then applied to the simulated image.

Figures A17–A22 illustrate the PSR boundary, maximum surface temperature outlines, and coronene surface stability outlines for every crater not showcased in Section 3.2. The transects used for Figure 10 are displayed as blue rectangles in Figures 6, 9, A8, A17–A20, and A22.
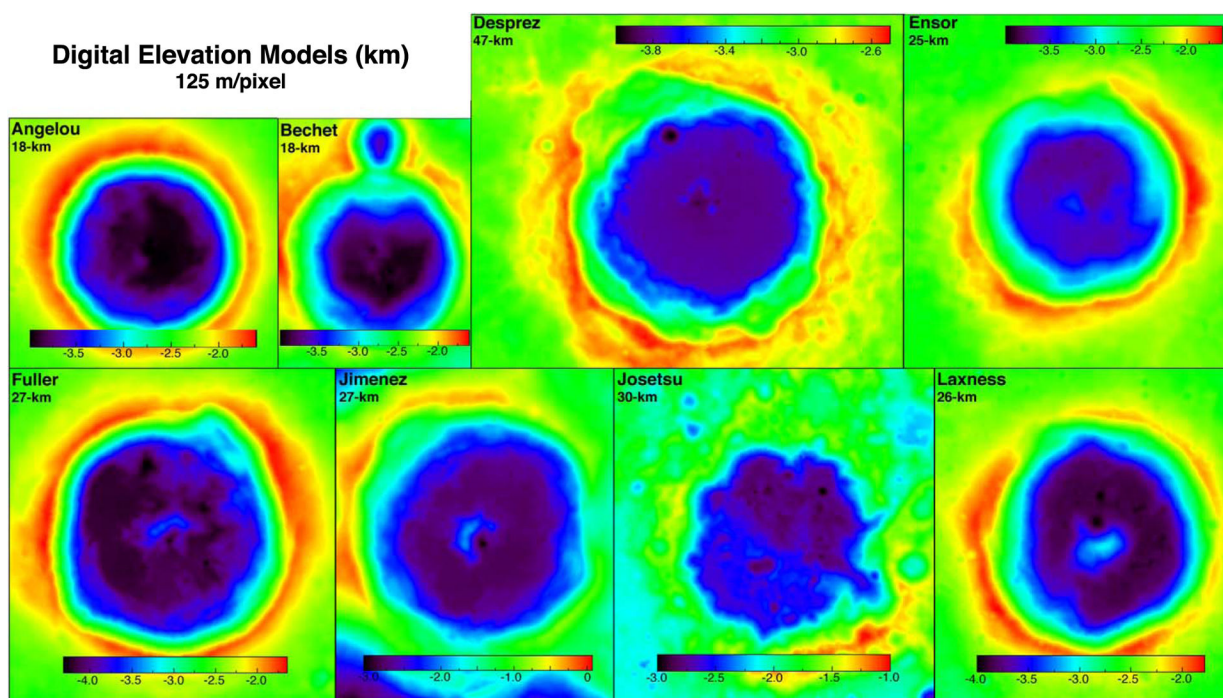
Figure A1.
All high-resolution (125 m pixel^{-1}) DEMs made for this study of Mercury's north polar deposits. These DEMs were made using a combination of MLA data and SfS techniques using MDIS images.
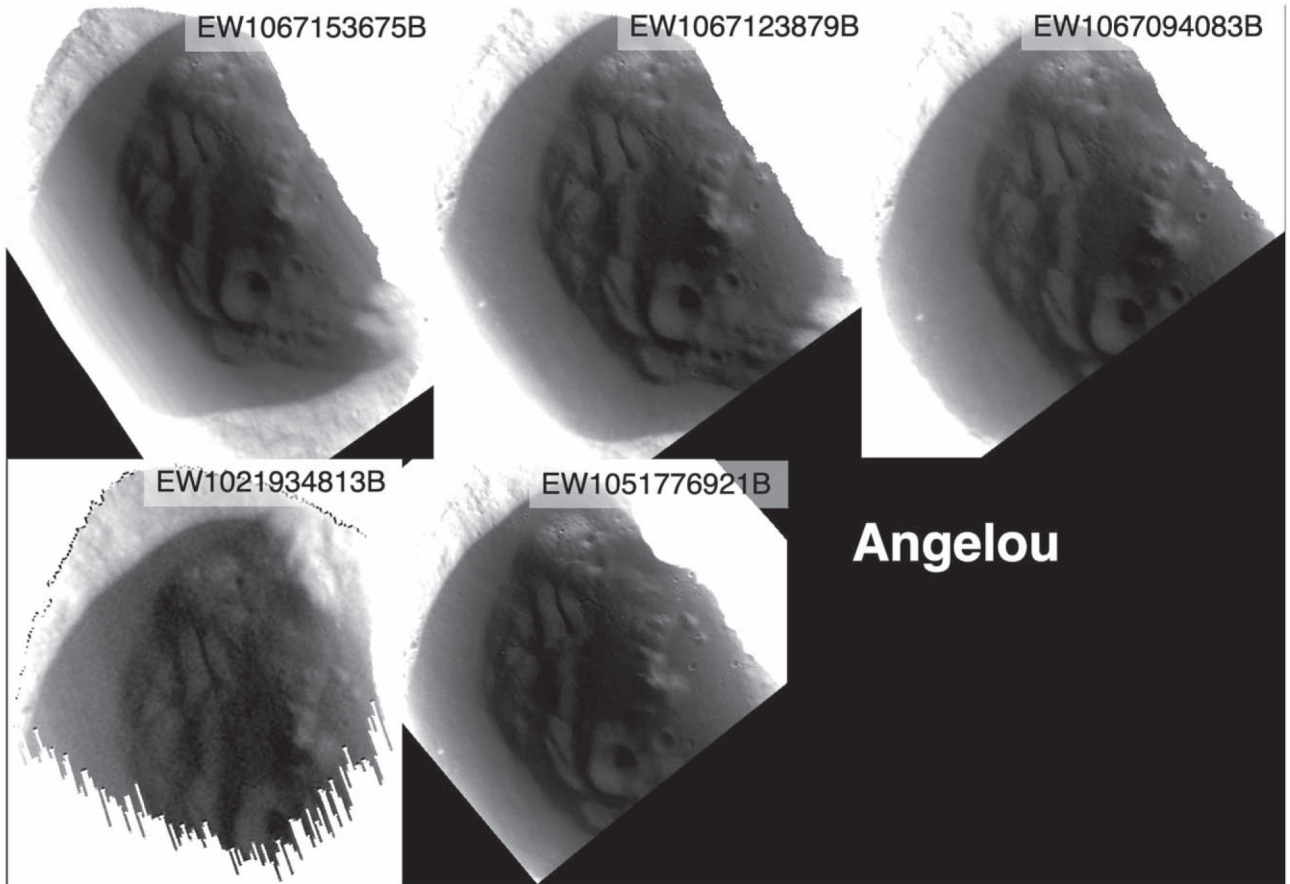
Figure A2.
All WAC broadband images gathered for Angelou (18 km diameter).
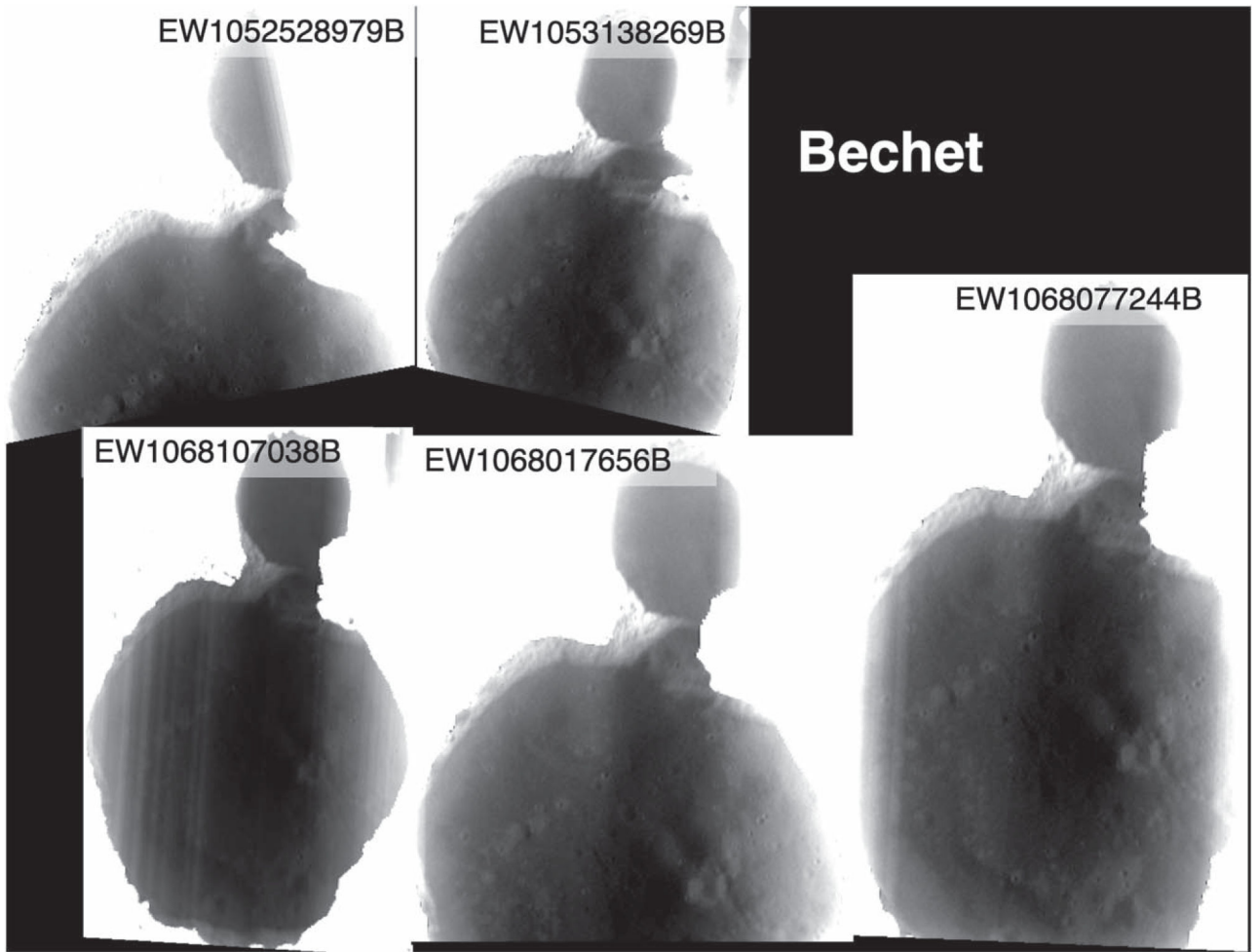
Figure A3.
All WAC broadband images gathered for Bechet (18 km diameter).
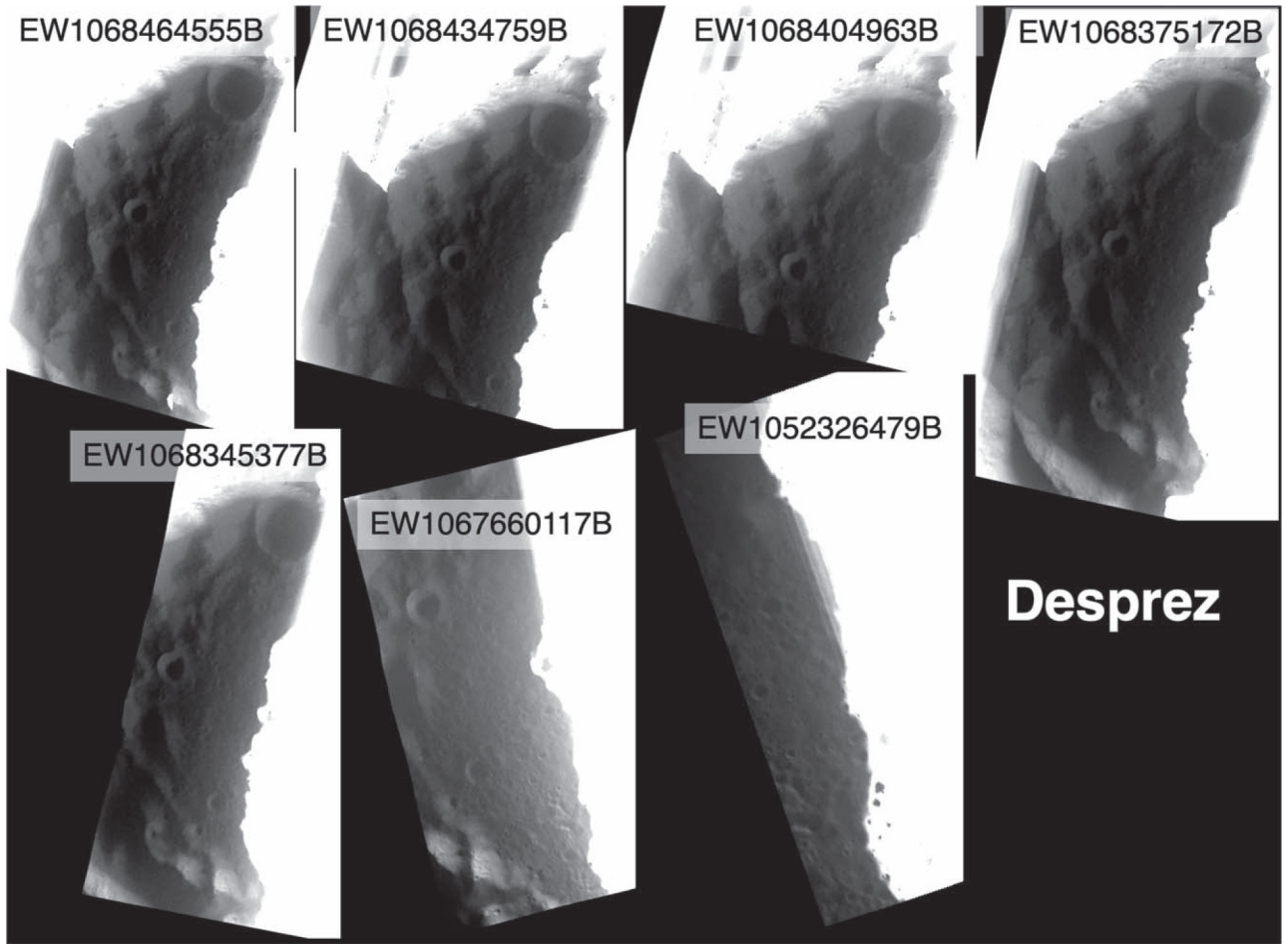
Figure A4.
All WAC broadband images gathered for Desprez (47 km diameter).
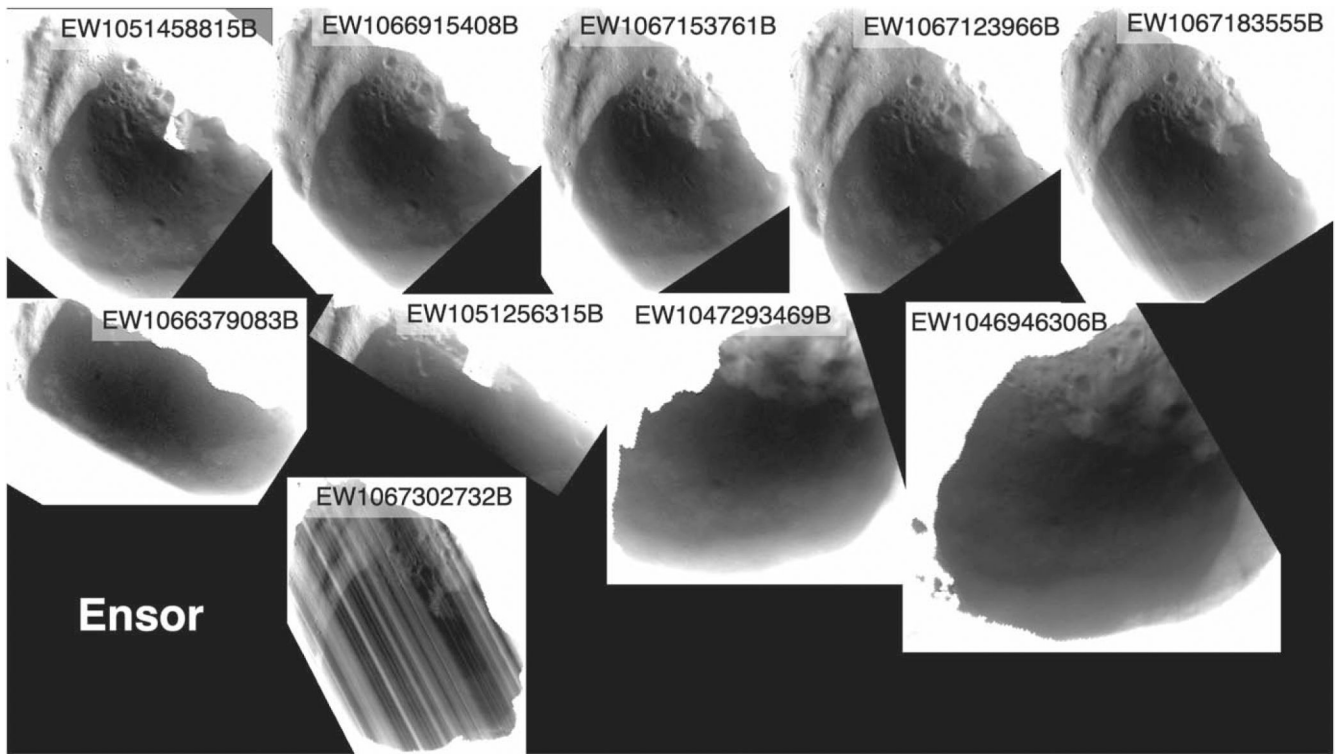
Figure A5.
All WAC broadband images gathered for Ensor (25 km diameter).
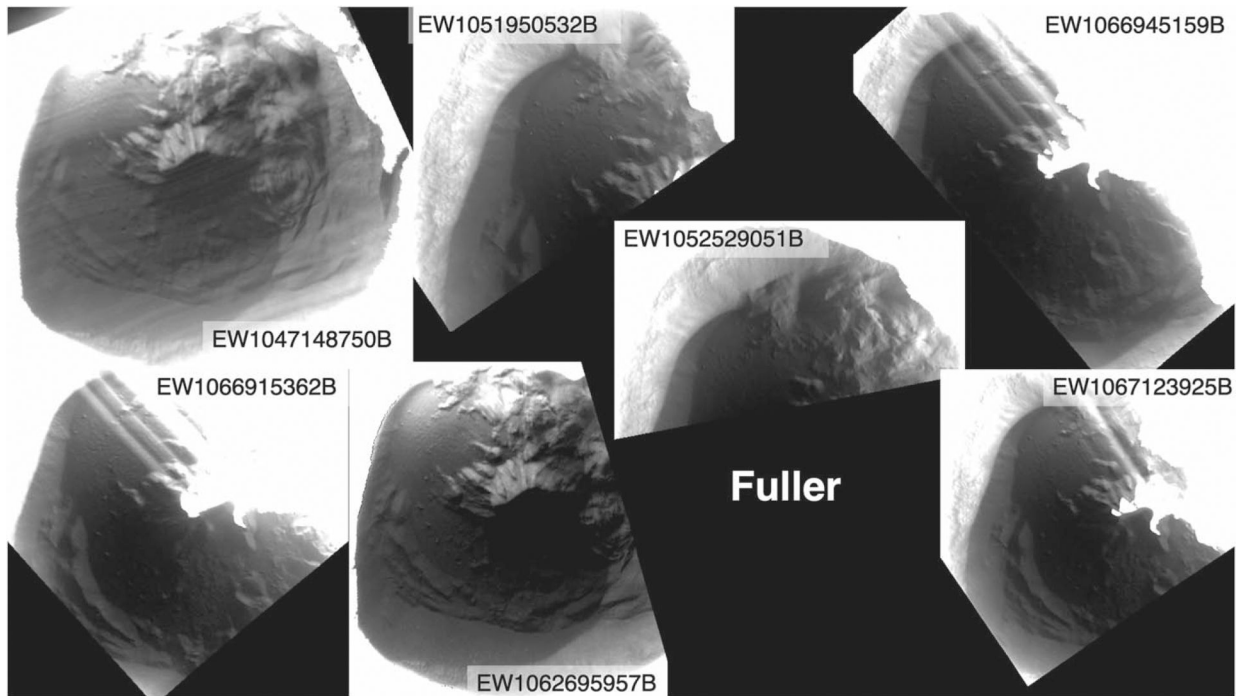
Figure A6.
All WAC broadband images gathered for Fuller (27 km diameter).
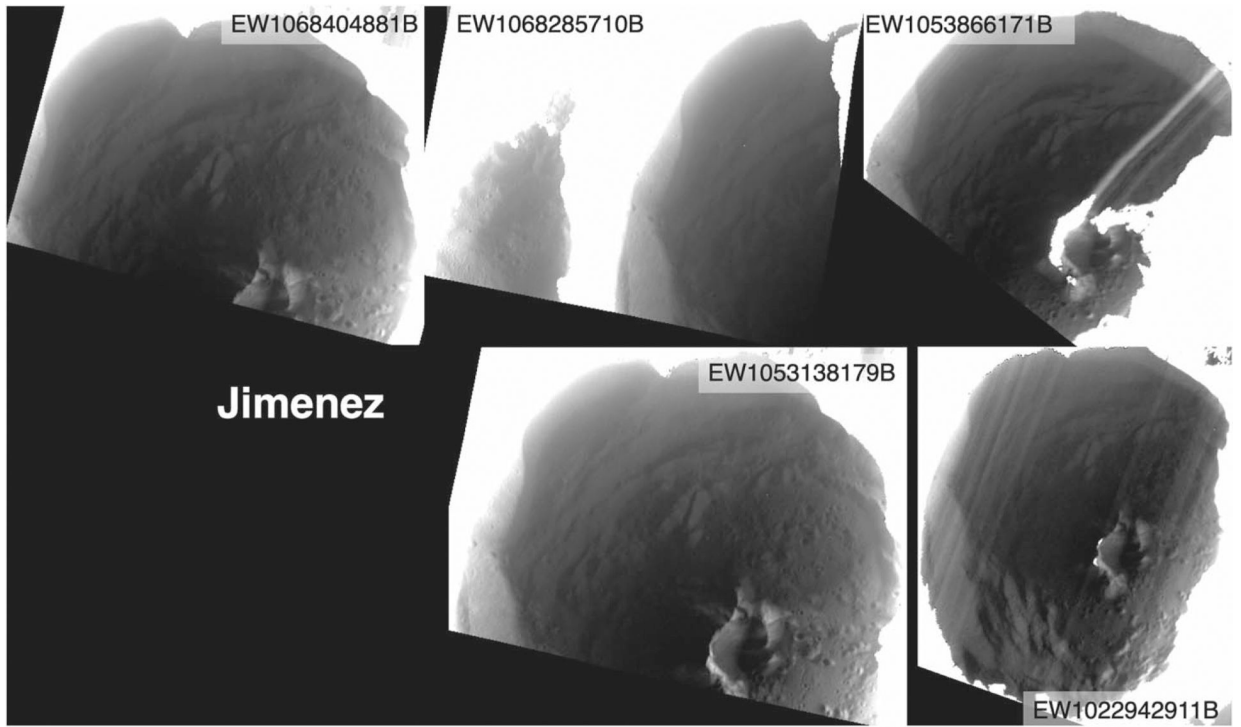
Figure A7.
All WAC broadband images gathered for Jimenez (27 km diameter).

EW1053138212B EW1053225572B EW1068404915B EW1068434710B

EW1068464505B EW1068732651B
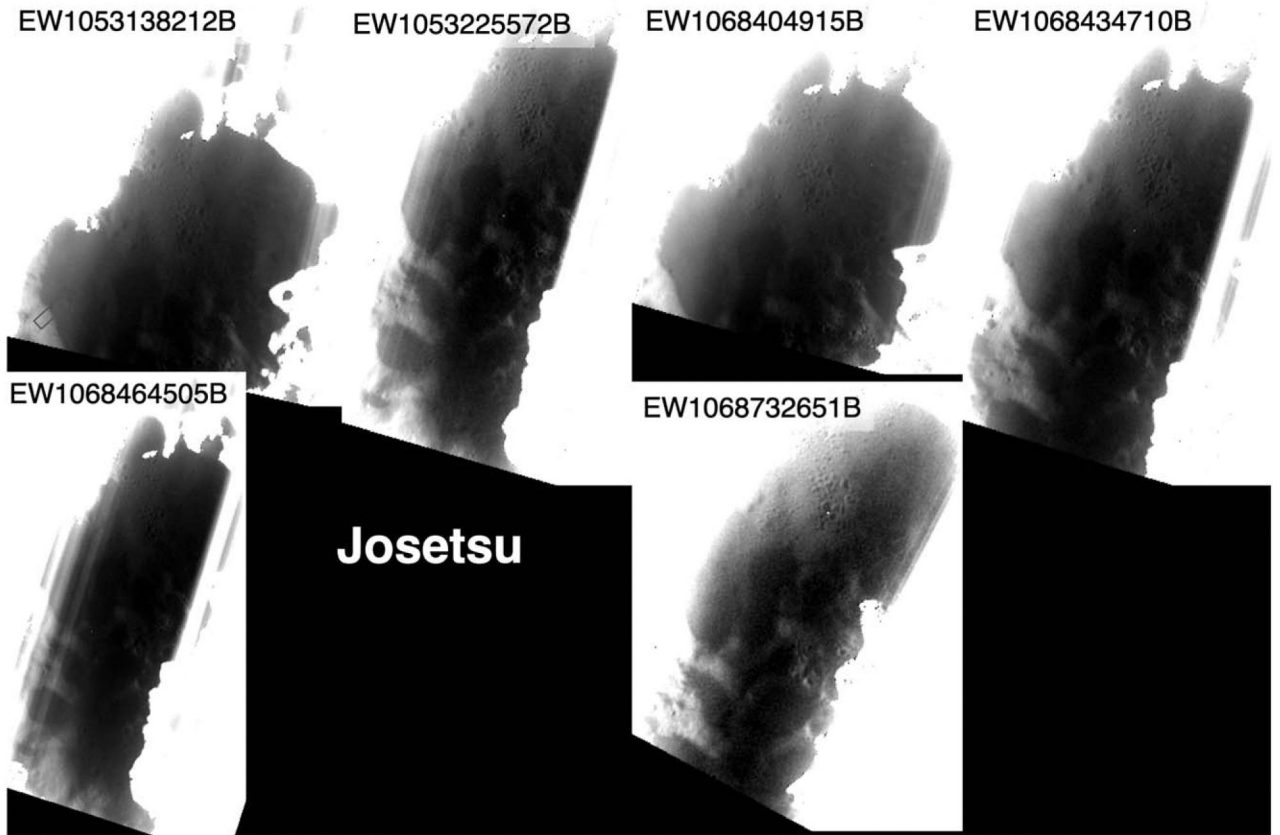
Josetsu

Figure A8.
All WAC broadband images gathered for Josetsu (30 km diameter). The blue rectangle in the first image denotes the transect used in Figure 11(g).
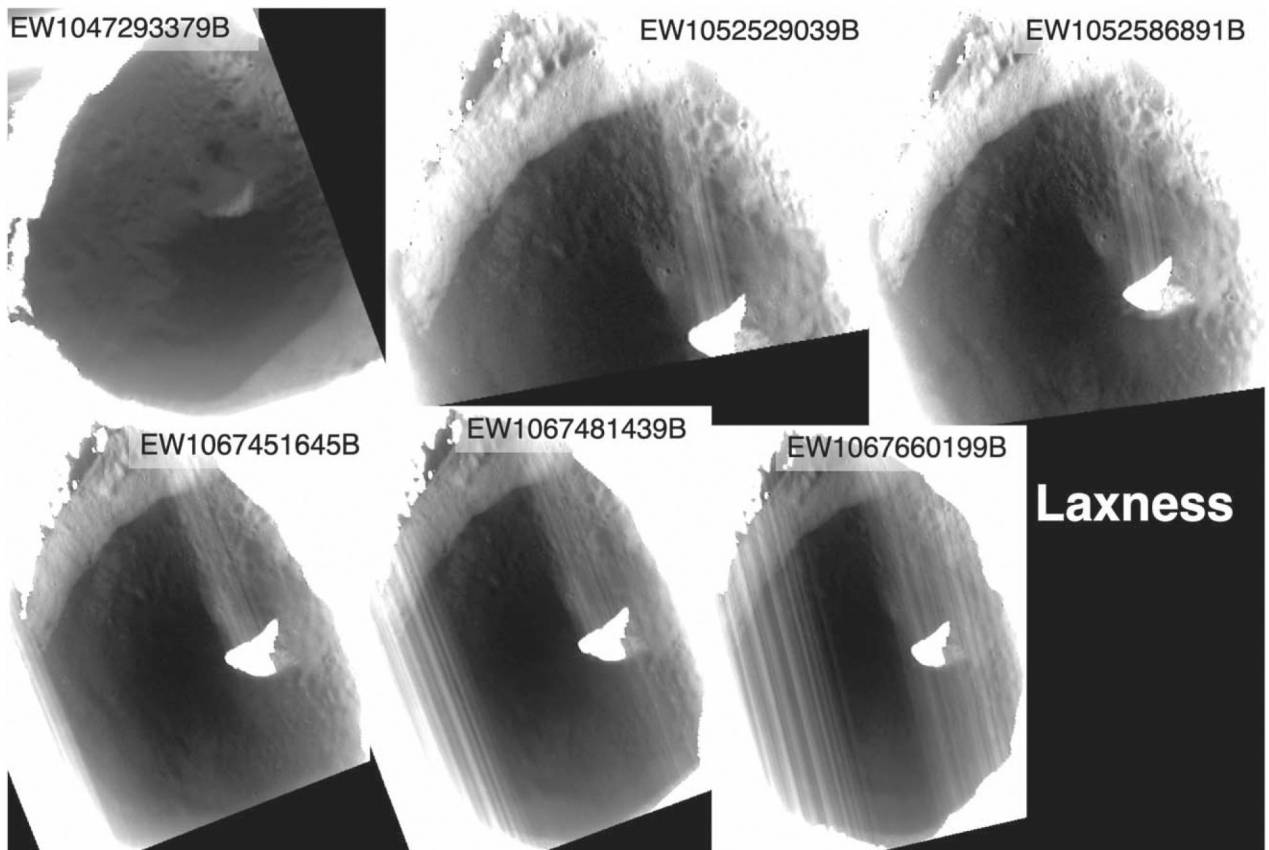
Figure A9.
All WAC broadband images gathered for Laxness (26 km diameter).
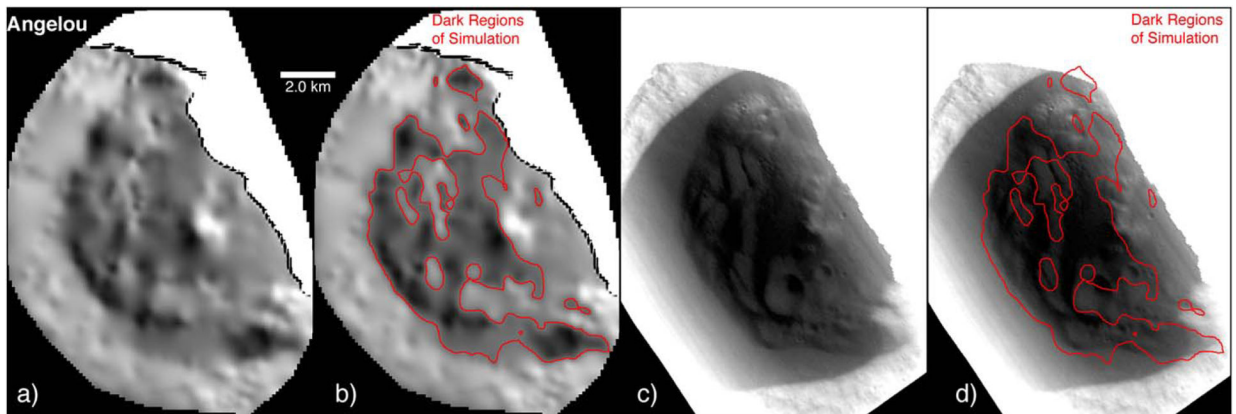
Figure A10.
(a) Simulated image for EW1067153675B of Angelou (18 km diameter) at 125 m pixel^{-1}, (b) with dark regions outlined in red. (c) WAC broadband image EW1067153675B (24 m pixel^{-1}) of Angelou, (d) with dark regions outlined from the simulated image overlaid on top of the WAC image (red).
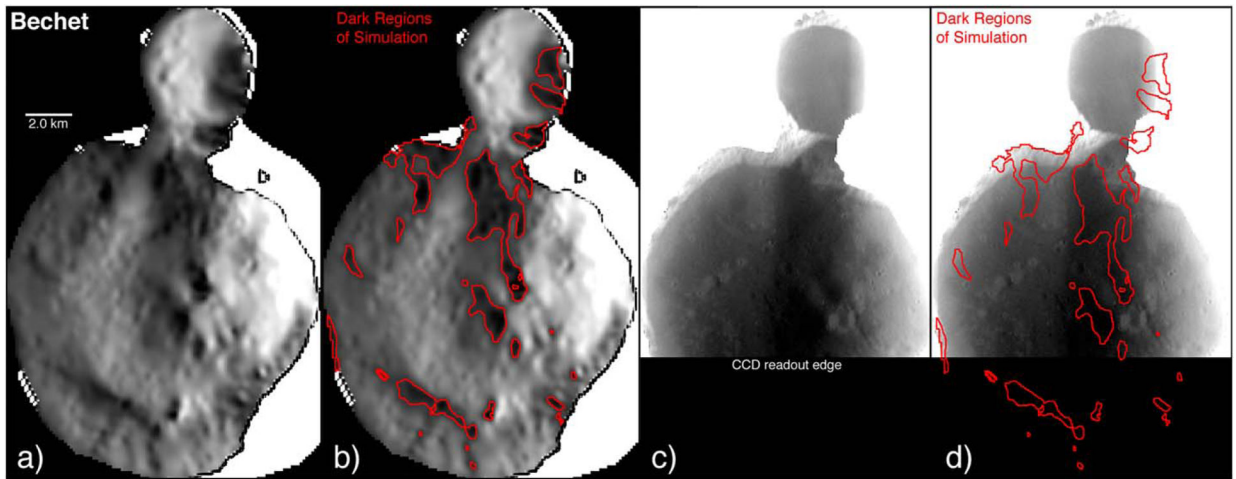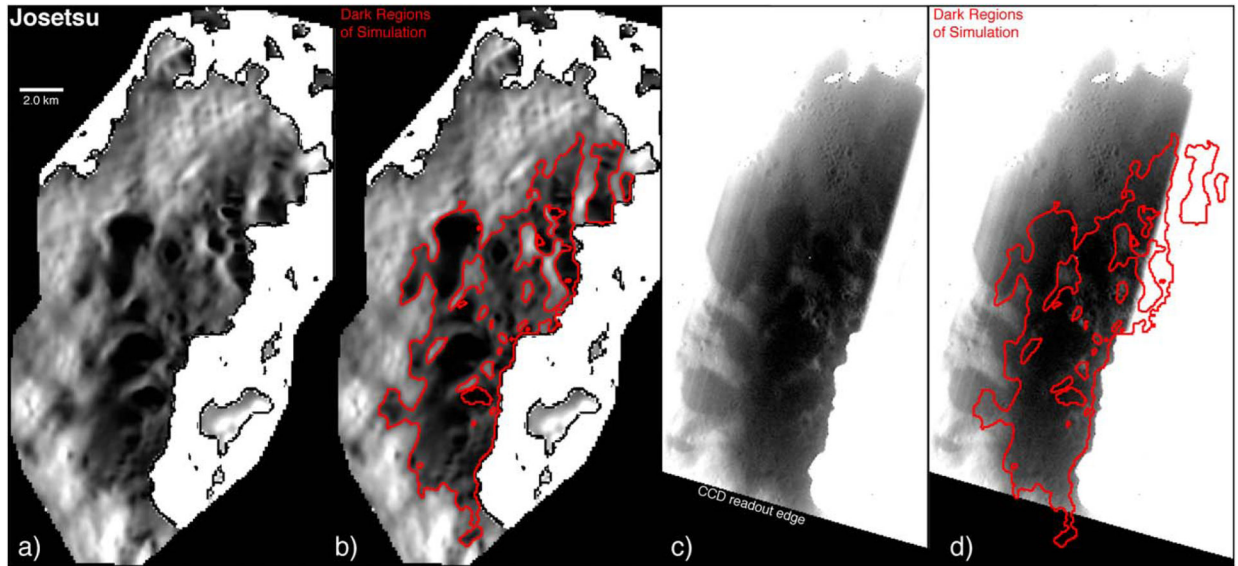
Figure A11.
(a) Simulated image for EW1068017656B of Bechet (18 km diameter) at 125 m pixel^{-1}, (b) with dark regions outlined in red. (c) WAC broadband image EW1068017656B (56 m pixel $^{-1}$) of Bechet, (d) with dark regions outlined from the simulated image overlaid on top of the WAC image (red).
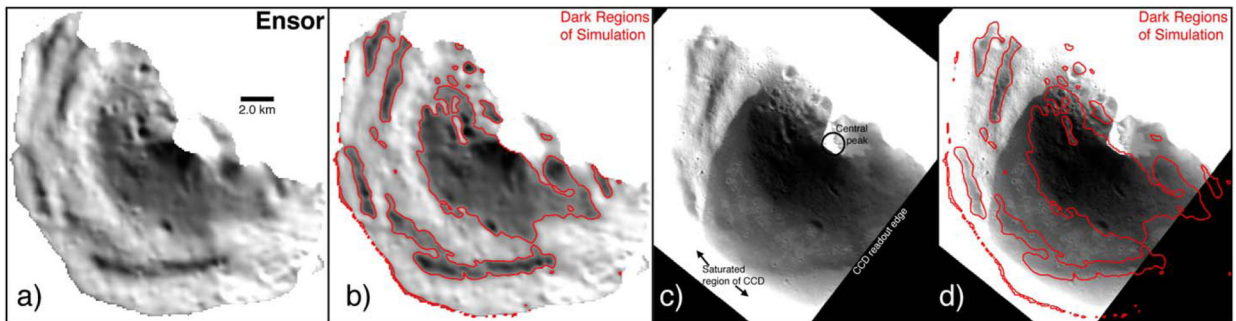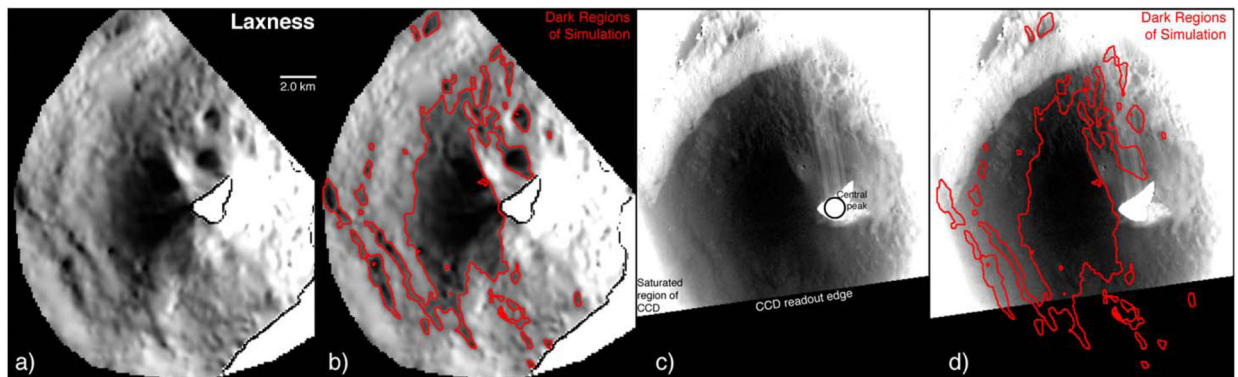

Figure A12.
(a) Simulated image for EW1051458815B of Ensor (25 km diameter) at 125 m pixel^{-1}, (b) with dark regions outlined in red. (c) WAC broadband image EW1051458815B (38 m pixel $^{-1}$) of Ensor, (d) with dark regions outlined from the simulated image overlaid on top of the WAC image (red).
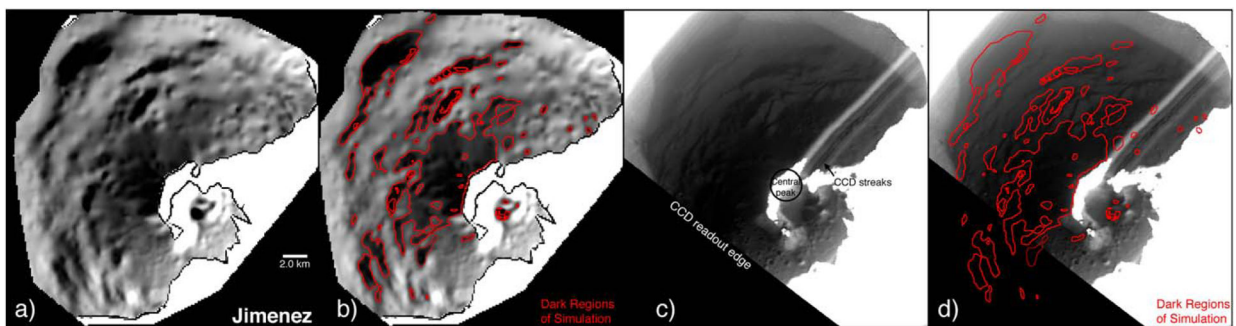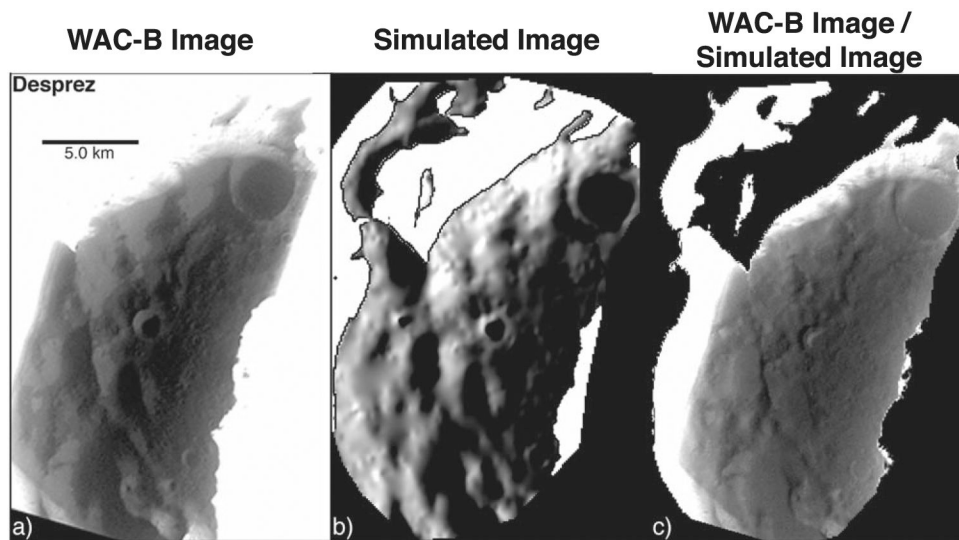

Figure A13.

(a) Simulated image for EW1053866171B of Jimenez (27 km diameter) at 125 m pixel^{-1}, (b) with dark regions outlined in red. (c) WAC broadband image EW1053866171B (75 m pixel^{-1}) of Jimenez, (d) with dark regions outlined from the simulated image overlaid on top of the WAC image (red).

Figure A14.
(a) Simulated image for EW1053225572B of Josetsu (30 km diameter) at 125 m pixel^{-1}, (b) with dark regions outlined in red. (c) WAC broadband image EW1053225572B (61 m pixel $^{-1}$) of Josetsu, (d) with dark regions outlined from the simulated image overlaid on top of the WAC image (red).

Figure A15.
(a) Simulated image for EW1052586891B of Laxness (26 km diameter) at 125 m pixel^{-1}, (b) with dark regions outlined in red. (c) WAC broadband image EW1052586891B (48 m pixel^{-1}) of Laxness, (d) with dark regions outlined from the simulated image overlaid on top of the WAC image (red).

WAC-B Image **Simulated Image** **WAC-B Image / Simulated Image**

Figure A16.

(a) WAC broadband image EW1068375172B of Desprez (47 km diameter) and (b) simulated image for the same image of Desprez. (c) A ratio (WAC image divided by simulated image) that shows how the simulated image predicts the brightness variations within Desprez' low-reflectance polar deposit.
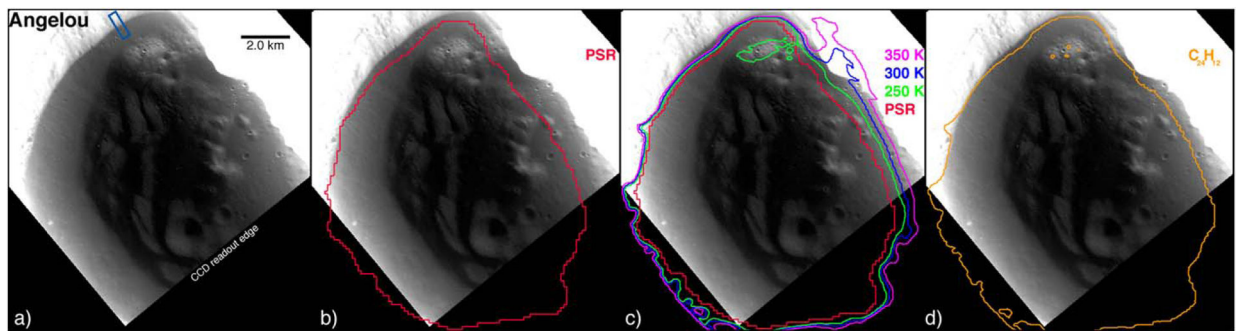

Figure A17.

(a) WAC broadband image EW1051776921B (24 m pixel^{-1}) of Angelou's low-reflectance polar deposit. The blue rectangle denotes the transect used in Figure A1(a). (b) Outline of Angelou's PSR (red). (c) Outline of PSR (red) and 250, 300, and 350 K maximum surface temperatures (green, blue, and purple). (d) Outline of region where coronene ($C_{24}H_{12}$) is thermally stable on the surface (orange).
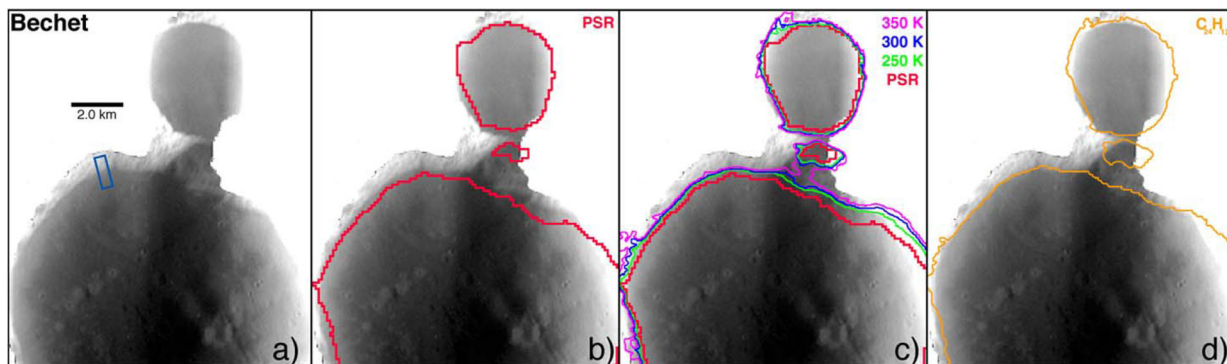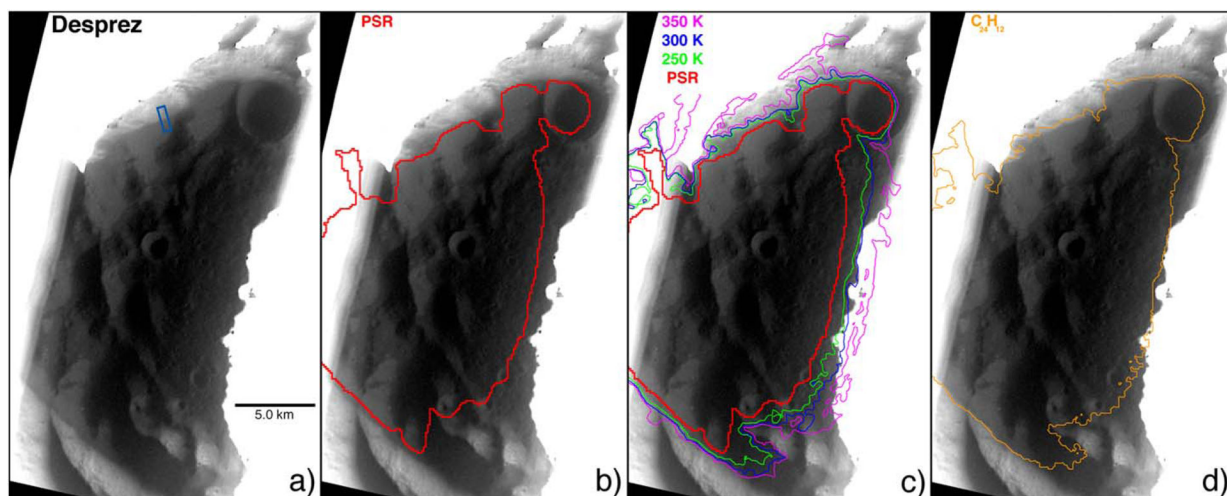
Figure A18.
(a) WAC broadband image EW1068017656B (56 m pixel^{-1}) of Bechet's low-reflectance polar deposit. The blue rectangle denotes the transect used in Figure A1(b). (b) Outline of Bechet's PSR (red). (c) Outline of PSR (red) and 250, 300, and 350 K maximum surface temperatures (green, blue, and purple). (d) Outline of region where coronene ($C_{24}H_{12}$) is thermally stable on the surface (orange).

Figure A19.
(a) WAC broadband image EW1068375172B (72 m pixel^{-1}) of Desprez' low-reflectance polar deposit. The blue rectangle denotes the transect used in Figure A1(c). (b) Outline of Desprez' PSR (red). (c) Outline of PSR (red) and 250, 300, and 350 K maximum surface temperatures (green, blue, and purple). (d) Outline of region where coronene ($C_{24}H_{12}$) is thermally stable on the surface (orange).
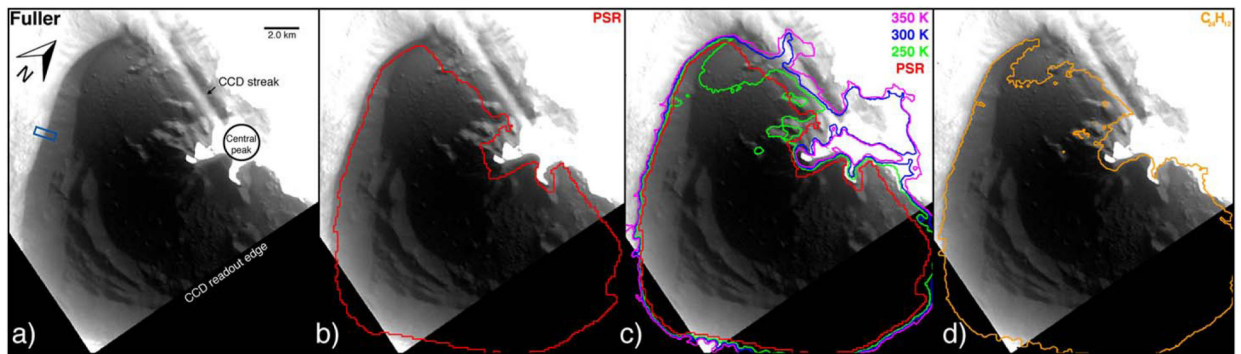
Figure A20.
(a) WAC broadband image EW1067123925B (51 m pixel^{-1}) of Fuller's low-reflectance polar deposit. The blue rectangle denotes the transect used in Figure A1(e). (b) Outline of Fuller's PSR (red). (c) Outline of PSR (red) and 250, 300, and 350 K maximum surface temperatures (green, blue, and purple). (d) Outline of region where coronene ($C_{24}H_{12}$) is thermally stable on the surface (orange).
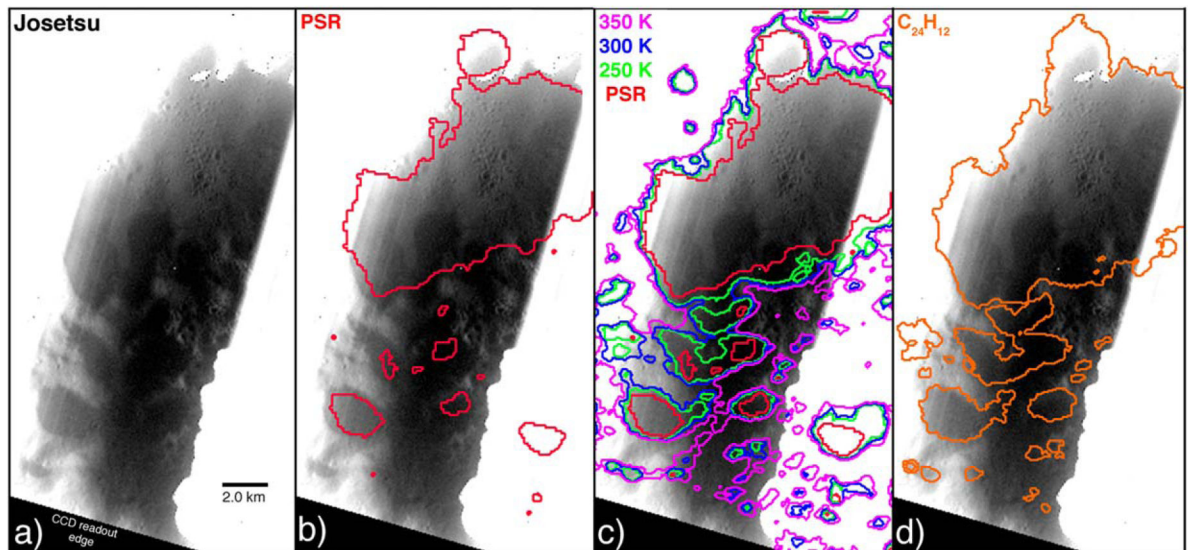

Figure A21.
(a) WAC broadband image EW1053225572B (61 m pixel^{-1}) of Josetsu's low-reflectance polar deposit. (b) Outline of Josetsu's PSR (red). (c) Outline of PSR (red) and 250, 300, and 350 K maximum surface temperatures (green, blue, and purple). (d) Outline of region where coronene ($C_{24}H_{12}$) is thermally stable on the surface (orange).
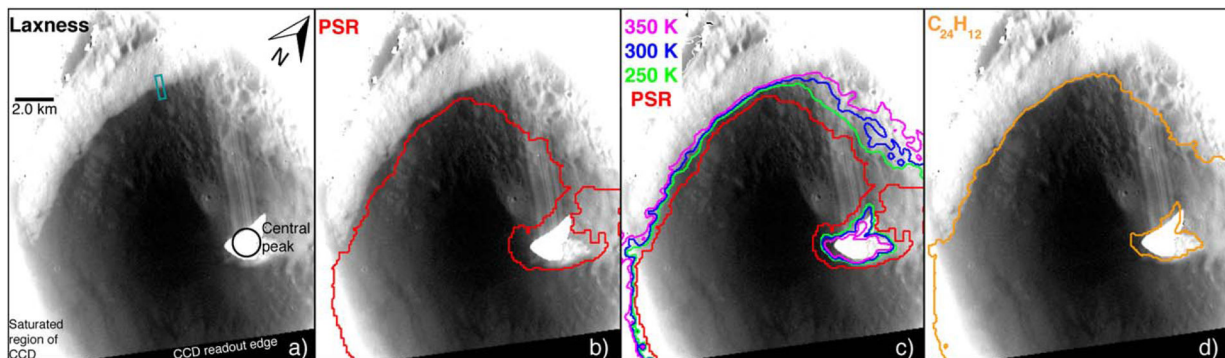
Figure A22.

(a) WAC broadband image EW1052586891B (48 m pixel^{-1}) of Laxness' low-reflectance polar deposit. The blue rectangle denotes the transect used in Figure A1(h). (b) Outline of Laxness' PSR (red). (c) Outline of PSR (red) and 250, 300, and 350 K maximum surface temperatures (green, blue, and purple). (d) Outline of region where coronene ($C_{24}H_{12}$) is thermally stable on the surface (orange).

Table A1

Catalog of WAC Broadband Images and WAC Narrowband Images Used for Each Crater

Image	Resolution (m pixel^{-1})	Emission angle (deg)	Incidence angle (deg)	Phase angle (deg)
Angelou				
EW1051776921B	24.3	6.3	80.6	74.4
EW1067094083B	39.9	15.8	80.5	96.3
EW1067123879B	42.1	20.4	80.5	100.9
EW1067153675B	44.0	22.6	80.6	103.2
EW1021934813B	75.3	22.8	80.4	103.2
EW0242004745G	131.2	0.2	80.3	80.4
Bechet				
EW1052528979B	32.6	3.1	83.3	80.2
EW1068017656B	55.8	1.2	83.1	84.3
EW1068077244B	58.0	1.1	83.1	84.2
EW1068107038B	59.0	0.8	83.1	83.9
EW1053138269B	71.5	0.9	83.2	84.1
EW0242589668G	123.7	7.3	83.5	76.2
Desprez				
EW1052326479B	25.5	5.1	82.3	77.2
EW1067660117B	42	12.9	81.9	94.8
EW1068345377B	68.6	22.9	81.3	104.2
EW1068375172B	70.3	23.5	81.1	104.6
EW1068404963B	70.5	23.6	81.1	104.7
EW1068434759B	71.5	21.8	81.1	102.9
EW1068464555B	72.4	20.0	81.1	101.1
EW0213416366G	156.7	0.7	81.6	82.3

Image	Resolution (m pixel^{-1})	Emission angle (deg)	Incidence angle (deg)	Phase angle (deg)
Ensor				
EW1051256315B	32.6	16.4	82.7	66.3
EW1051458815B	37.9	20.1	82.9	103.0
EW1066379083B	48.5	33.8	82.5	48.7
EW1066915408B	58.9	13.1	83.5	96.6
EW1067123966B	63.6	8.3	84.0	92.4
EW1067153761B	64.7	7.5	84.2	91.6
EW1067183555B	65.4	6.1	84.3	90.3
EW1067302732B	69.2	0.1	84.8	84.8
EW1047293469B	90.2	0.2	83.6	83.7
EW1046946306B	91.4	34.0	84.3	118.3
EW1005112163G	91.6	28.2	82.6	85.5
Fuller				
EW1051950532B	37.9	16.6	82.9	99.5
EW1066915362B	45.9	10.5	82.7	72.2
EW1066945159B	46.9	7.4	82.8	75.4
EW1062695957B	47.2	42.4	85.7	128.1
EW1052529051B	48.9	0.8	84.1	83.5
EW1067123925B	51.4	4.2	82.9	87.1
EW1047148750B	90.1	39.2	86.7	125.9
EW0241545232G	67.7	28.4	83.1	83.8
Jimenez				
EW1068285710B	40.4	5.9	84.6	78.7
EW1068404881B	42.4	4.0	84.4	88.4
EW1053138179B	52.7	0.4	84.7	85.1
EW1022942911B	70.5	11.7	83.6	95.3
EW1053866171B	74.5	26.2	82.4	108.6
EW0244516343G	106.2	0.2	81.9	81.8
Josetsu				
EW1068404915B	51.4	5.4	84.1	78.8
EW1068434710B	52.6	5.3	84.1	78.8
EW1068464505B	53.7	4.5	84.0	79.5
EW1053138212B	59.0	2.9	84.3	81.5
EW1053225572B	61.1	0.2	84.1	84.3
EW1068732651B	61.4	3.8	83.6	79.7
EW0259292783G	75.4	10.2	83.7	83.8
Laxness				
EW1052529039B	46.0	4.4	84.2	79.8
EW1052586891B	47.8	7.0	84.3	77.2
EW1067451645B	57.2	3.6	83.7	80.1
EW1067481439B	58.2	3.9	83.7	79.9

Image	Resolution (m pixel^{-1})	Emission angle (deg)	Incidence angle (deg)	Phase angle (deg)
EW1067660199B	63.9	7.2	84.0	76.8
EW1047293379B	87.3	36.5	87.3	123.8
EW0242255486G	58.5	0.2	83.6	83.7

Note. The broadband images are ordered by their resolution, and the narrowband image is last for every crater.

References

Alexandrov O, & Beyer RA 2018, E&SS, 5, 652

Beyer RA, Alexandrov O, & McMichael S 2018, E&SS, 5, 537

Botta O, & Bada JL 2002, SGeo, 23, 411

Butler BJ, Muhleman DO, Slade MA, et al. 1993, JGR, 98, 15003

Cavanaugh JF, Smith JC, Sun X, et al. 2007, SSRv, 131, 451

Chabot NL, Ernst CM, Denevi BW, et al. 2012, GeoRL, 39, L09204

Chabot NL, Ernst CM, Denevi BW, et al. 2014, Geo, 42, 1051

Chabot NL, Ernst CM, Harmon JK, et al. 2013, JGR, 118, 26

Chabot NL, Ernst CM, Paige DA, et al. 2016, GeoRL, 43, 9461

Chabot NL, Lawrence DJ, Neumann GA, et al. 2018a, in Mercury: The View After MESSENGER, ed. Solomon SC et al. (Cambridge: Cambridge Univ. Press), 13

Chabot NL, Shread EE, & Harmon JK 2018b, JGR, 123, 666

Clemett SJ, Sandford SA, Nakamura-Messenger K, et al. 2010, M&PS, 45, 701

Clemett SJ, & Zare RN 1997, in Proc. IAU Symp. 178, ed. van Dishoeck EF (Cambridge: Cambridge Univ. Press), 305

Colombo G, & Shapiro II 1966, ApJ, 145, 296

Crites ST, Lucey PG, & Lawrence DJ 2013, Icar, 226, 1192

Delitsky ML, Paige DA, Siegler MA, et al. 2017, Icar, 281, 19

Denevi BW, Chabot NL, Murchie SM, et al. 2018, SSRv, 214, 2

Deutsch AN, Chabot NL, Mazarico EM, et al. 2016, Icar, 280, 158

Deutsch AN, Head JW, & Neumann GA 2019, E&PSL, 520, 26

Deutsch AN, Neumann GA, & Head JW 2017, GeoRL, 44, 9233

Domingue DL, D'Amore M, Ferrari S, et al. 2019, Icar, 319, 247

Filacchione G, Frigeri A, Raponi A, et al. 2020, MNRAS, 498, 1308

Gaddis LR, Becker K, Becker T, et al. 1997, LPI, 28, 387

Harmon JK 2007, SSRv, 132, 307

Harmon JK, Perillat PJ, Slade MA, et al. 2001, Icar, 149, 1

Harmon JK, & Slade MA 1992, Sci, 23, 640

Harmon JK, Slade MA, & Rice MS 2011, Icar, 211, 37

Harmon JK, Slade MA, Velez RA, et al. 1994, Natur, 369, 213

Hawkins SE, Boldt JD, Darlington EH, et al. 2007, SSRv, 131, 247

Keys RG 1981, ITASS, 29, 1153

Kovalenko LJ, Philippoz JM, Bucenell JR, et al. 1991, SSRv, 56, 191

Lambert JH 1760, Photometry, or, On the Measure and Gradations of Light, Colors and Shade, Vol. 1 (1st ed.; Augsburg: Detleffsen)

Lawrence DJ, Feldman WC, Goldsten JO, et al. 2013, Sci, 339, 292

Mazarico E, Barker MK, & Nicholas JB 2018, AdSpR, 62, 3214

Mazarico E, Neumann GA, Smith DE, et al. 2011, Icar, 211, 1066

Mitchell DL, & Pater I 1994, Icar, 110, 2

Negi BS, Bhowmik NC, Mathur SS, et al. 1985, ApOpt, 24, 296

Neumann GA, Cavanaugh JF, Sun X, et al. 2013, Sci, 339, 296

Paige DA, Siegler MA, Harmon JK, et al. 2013, Sci, 339, 300

Paige DA, Wood SE, Vasavada AR, et al. 1992, Sci, 258, 643

Phillips RJ, Byrne PK, James PB, et al. 2018, in Mercury: The View After MESSENGER, ed. Solomon SC et al. (Cambridge: Cambridge Univ. Press), 3

Schorgofer N, & Taylor GJ 2007, E&SS, 112, E02010

Siegler MA, Paige DA, Williams JP, et al. 2014, Icar, 255, 78

Slade MA, Butler BJ, Muhleman DO, et al. 1992, Sci, 258, 635

Sprague AL, Hunten DM, & Lodders K 1995, Icar, 118, 211

Vasavada AR, Paige DA, & Wood SE 1999, Icar, 141, 179

Zhang JA, & Paige DA 2009, GeoRL, 36, L16203

Zhang JA, & Paige DA 2010, GeoRL, 37, L03203

Zuber MT, Head JW, Smith DE, et al. 2012, Natur, 486, 378

Mercury's North Polar Region
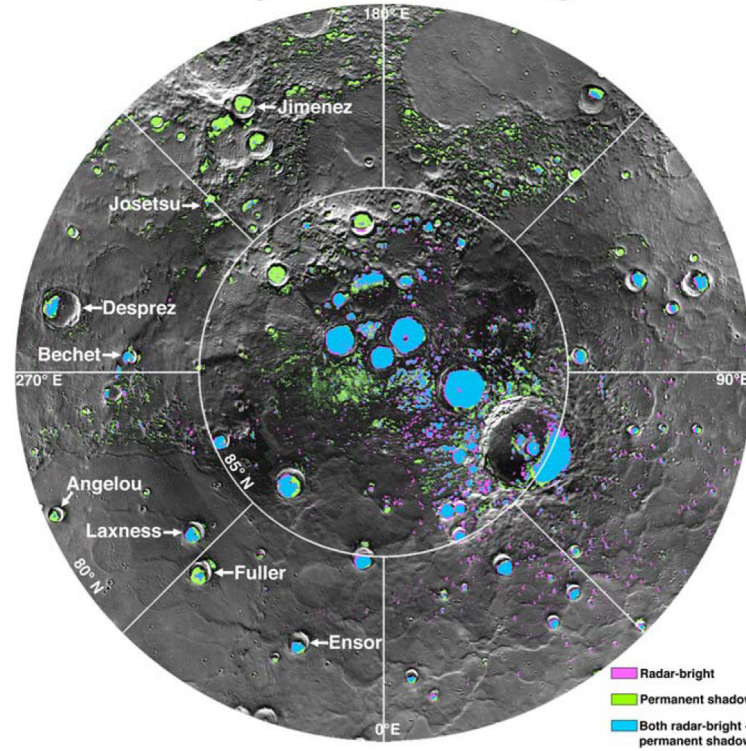
Figure 1.
Map of Mercury's north polar region with radar-bright-only regions (pink), regions of permanent shadow only (green), and regions that are both radar-bright and permanently shadowed (blue), from Deutsch et al. (2016). The eight craters investigated in this study are labeled.
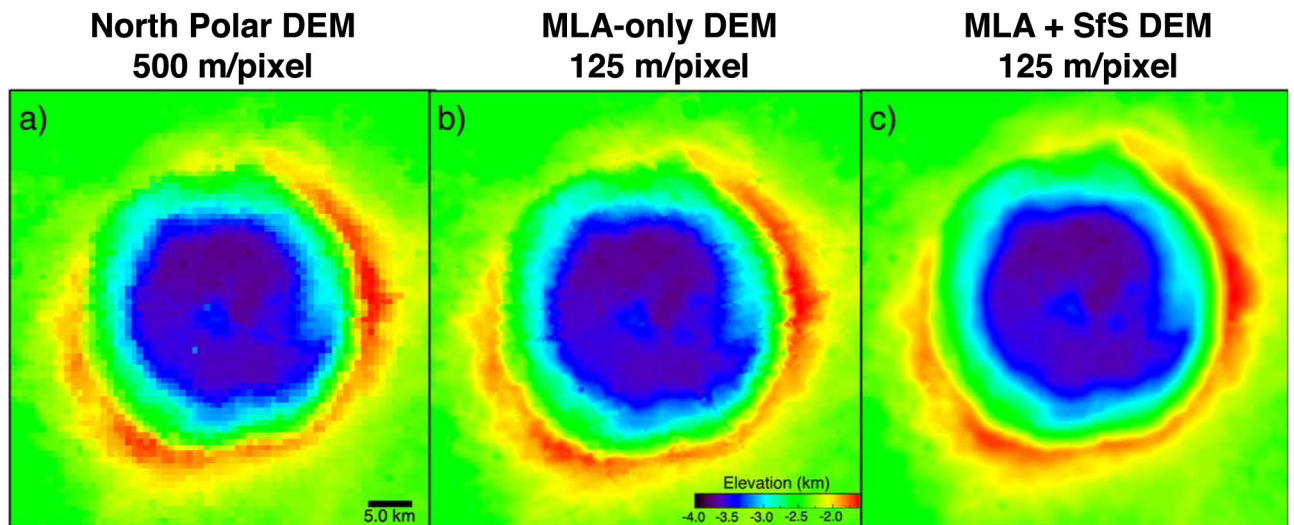
Figure 2.
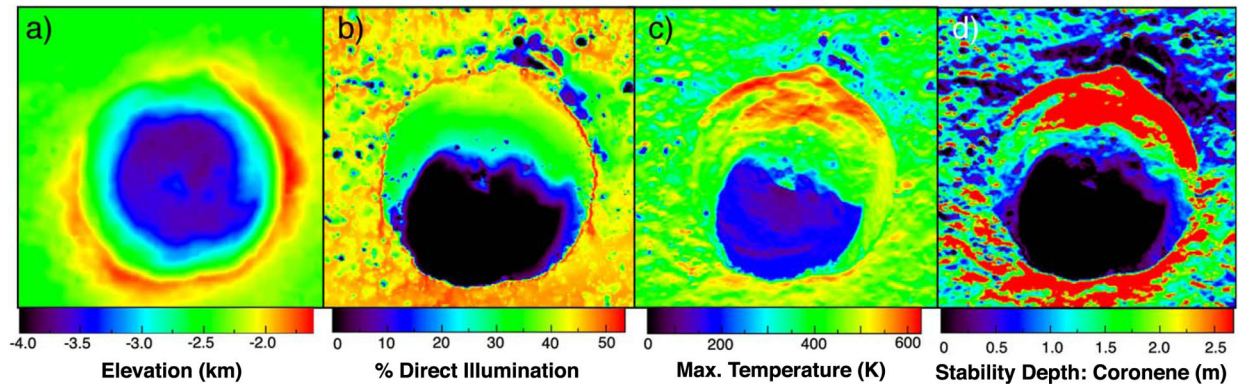DEMs of Ensor (25 km diameter). (a) North polar DEM at 500 m pixel^{-1}. (b) High-resolution DEM using MLA tracks only. (c) High-resolution DEM using MLA tracks and SfS.

Figure 3.
High-resolution models of Ensor (25 km diameter). (a) MLA + SfS DEM. (b) Average
illumination over one Mercury solar day. The majority of the black region represents the
PSR, as illustrated in Section 3.2. (c) Maximum surface temperature throughout a Mercury
solar day. (d) Depth below the surface needed for the long-term stability of coronene
($C_{24}H_{12}$). The black region represents where coronene is thermally stable at the surface.
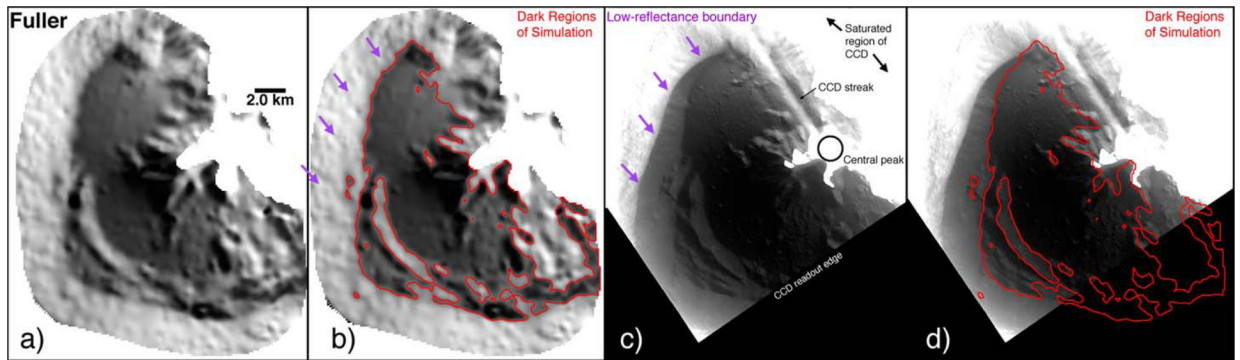
Figure 4.
(a) Simulated image for EW1067123925B of Fuller (27 km diameter) at 125 m pixel^{-1}, (b) with dark regions outlined in red. (c) WAC broadband image EW1067123925B (51 m pixel $^{-1}$) of Fuller, (d) with dark regions outlined from the simulated image overlaid on top of the WAC image (red). The purple arrows indicate the position of the polar deposit's low-reflectance boundary as seen in the WAC image.
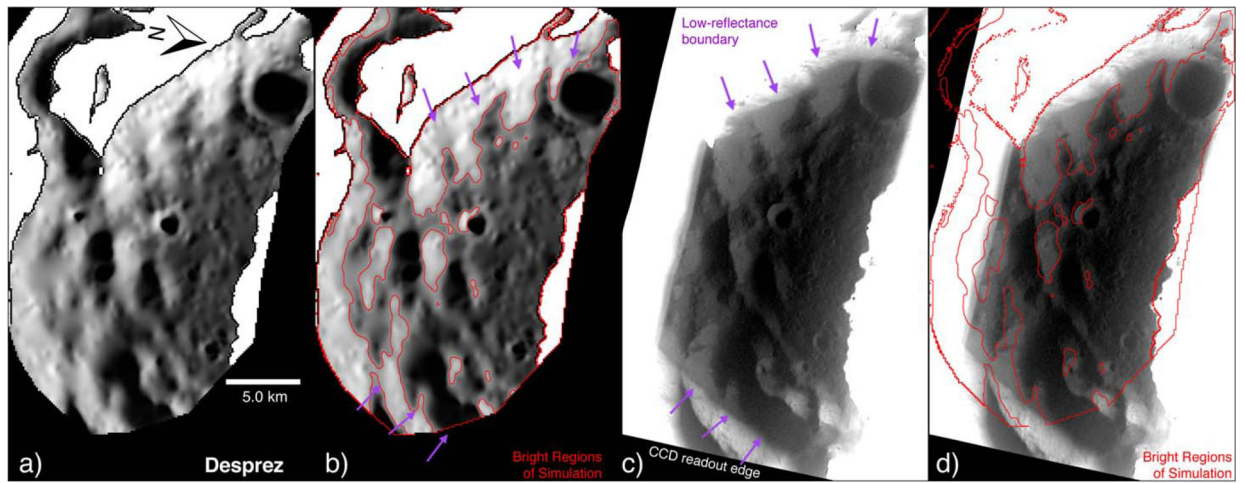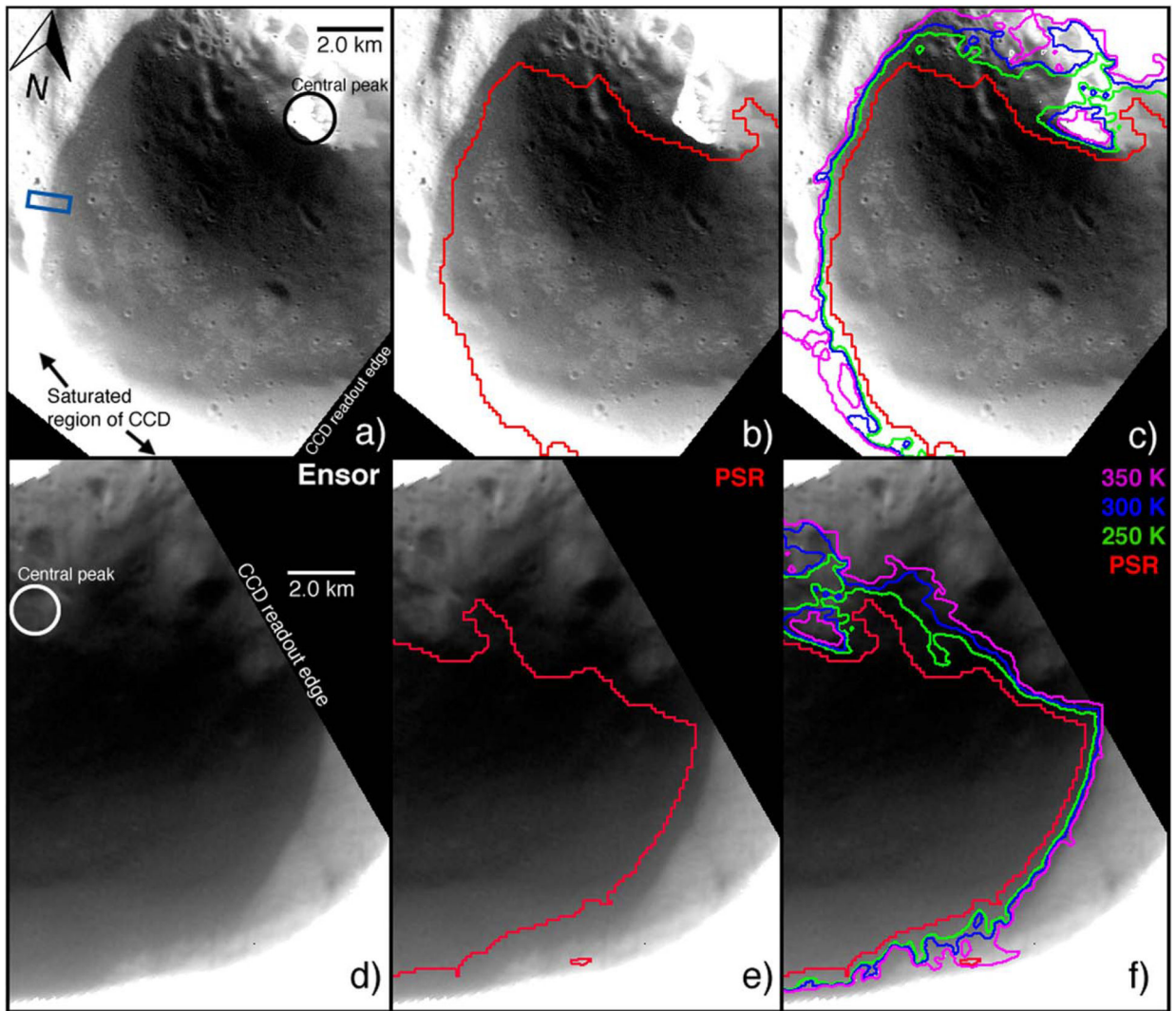
Figure 5.
(a) Simulated image for EW1068375172B of Desprez (47 km diameter) at 125 m pixel^{-1}, (b) with bright regions outlined in red. (c) WAC broadband image EW1068375172B (72 m pixel^{-1}) of Desprez, (d) with bright regions outlined from the simulated image overlaid on top of the WAC image (red). The purple arrows indicate the position of the polar deposit's low-reflectance boundary as seen in the WAC image.

Figure 6.
(a) WAC broadband image EW1051458815B (38 m pixel^{-1}) of Ensor's low-reflectance polar deposit. The blue rectangle denotes the transect used in Figure 10(d). (b) Outline of Ensor's PSR (red). (c) Outline of PSR (red) and 250, 300, and 350 K maximum surface temperatures for a Mercury solar day (green, blue, and purple). (d) WAC broadband image EW1046946306B of Ensor's low-reflectance polar deposit. (e) Outline of Ensor's PSR (red). (f) Outline of Ensor's PSR (red) and 250, 300, and 350 K maximum surface temperatures for a Mercury solar day (green, blue, and purple).
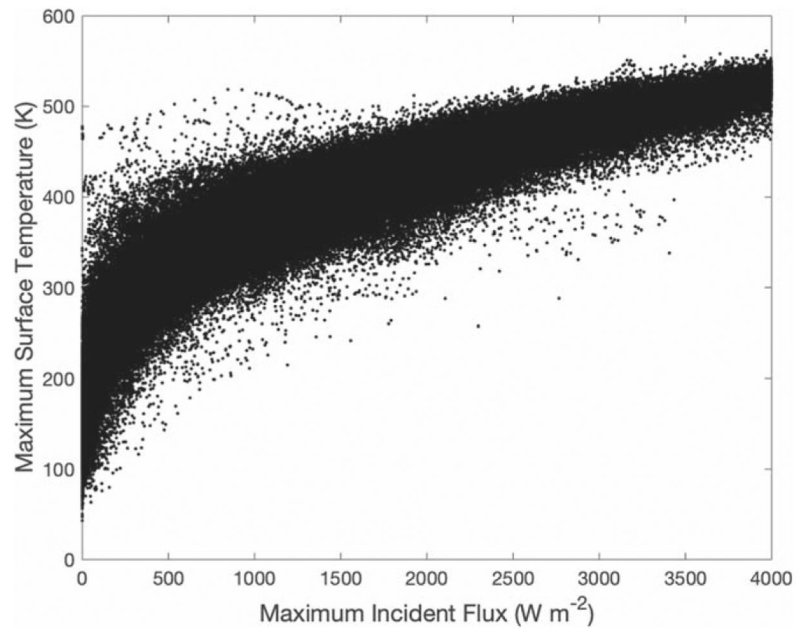
Figure 7.
Comparison of maximum incident flux (W m^{-2}) and maximum surface temperature (K) for the high-resolution models of Ensor.
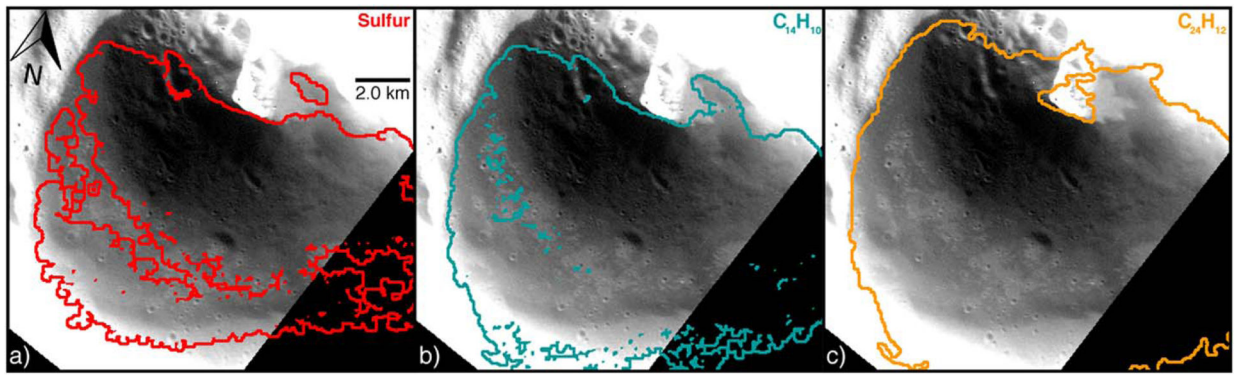
Figure 8.
WAC broadband image EW1051458815B (38 m pixel^{-1}) of Ensor. (a) Outline of region where sulfur (S) (red), (b) anthracene ($C_{14}H_{10}$) (blue), or (c) coronene ($C_{24}H_{12}$) (orange) is thermally stable on the surface.
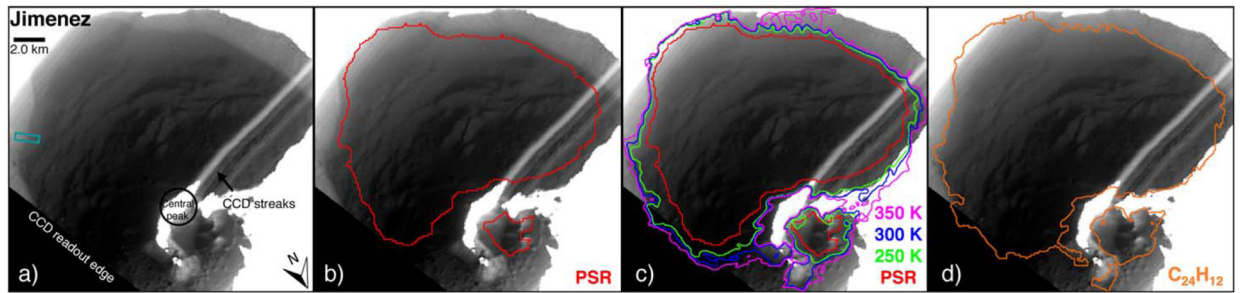
Figure 9.
(a) WAC broadband image EW1053866171B (75 m pixel^{-1}) of Jimenez's low-reflectance polar deposit. The blue rectangle denotes the transect used in Figure 10(f). (b) Outline of Jimenez's PSR (red). (c) Outline of PSR (red) and 250, 300, and 350 K maximum surface temperatures (green, blue, and purple). (d) Outline of region where coronene ($C_{24}H_{12}$) is thermally stable on the surface (orange).
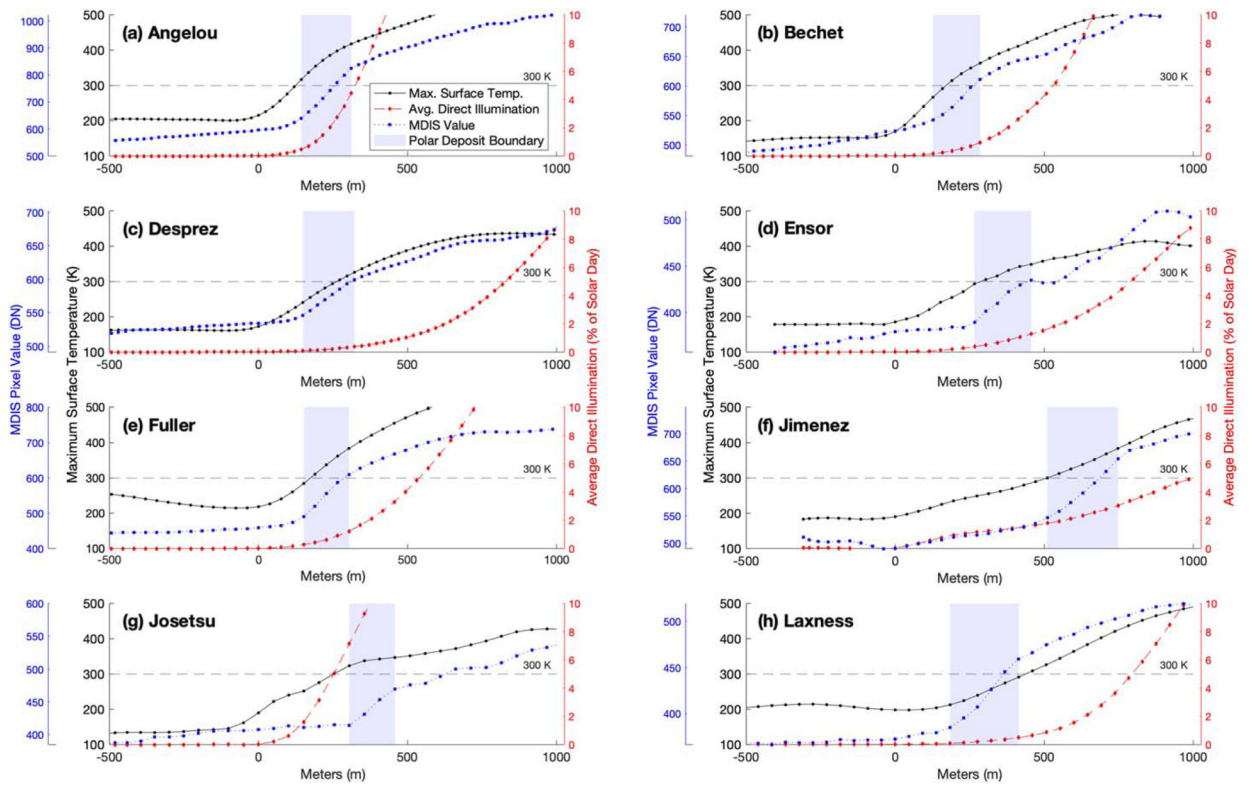
Figure 10.
Illumination and temperature conditions of Mercury's polar deposit boundaries for each crater studied. The boundary of the PSR is set at a distance of zero and derived from the average direct illumination model (red); the shaded region represents the location of the low-reflectance polar deposit boundary determined from the WAC broadband images in DN values (blue). The maximum surface temperatures (black) indicate that each polar deposit boundary corresponds roughly to 250–350 K.

Table 1

Names, Locations, and Diameters of All North Polar Craters Used in This Study of Mercury's Volatile Polar Deposits

Crater	Location	Diameter
Angelou	80.3°N, 293.3°E	18.0 km
Bechet	83.1°N, 266.3°E	17.6 km
Desprez	81.1°N, 258.7°E	47.1 km
Ensor	82.3°N, 342.5°E	24.8 km
Fuller	82.6°N, 317.4°E	27.0 km
Jimenez	81.8°N, 207.7°E	27.0 km
Josetsu	83.6°N, 225.6°E	30.0 km
Laxness	83.3°N, 310.0°E	25.9 km